https://doi.org/10.5194/os-2019-94
Preprint. Discussion started: 26 September 2019

Ocean Science
Discussions
Open Access

Internal tides in the Solomon Sea in contrasted ENSO conditions

Michel Tchilibou[1], Lionel Gourdeau[1], Florent Lyard[1], Rosemary Morrow[1], Ariane Koch Larrouy[1], Damien Allain[1], Bughsin Djath[2]

1) Laboratoire d'Etude en Géophysique et Océanographie Spatiales (LEGOS), Université de Toulouse, CNES, CNRS, IRD, UPS, Toulouse, France

2) Helmholtz-Zentrum Geesthacht Max-Planck-Strase, Geesthacht, Germany,

Contacts:
Michel tchilibou: michel.tchilibou@legos.obs-mip.fr
Lionel Gourdeau: lionel.gourdeau@legos.obs-mip.fr
Florent Lyard: florent.lyard@legos.obs-mip.fr
Rosemary Morrow: rosemary.morrow@legos.obs-mip.
Ariane.Koch-Larrouy@legos.obs-mip.fr
Damien.Allain@legos.obs-mip.fr
Bughsin Djath: nathachadjath@gmail.com

https://doi.org/10.5194/os-2019-94
Preprint. Discussion started: 26 September 2019

Ocean Science Discussions Open Access EGU

Abstract

The Solomon Sea is a place of intense Low Latitudes Western Boundary current transiting to the equator where mesoscale activity is superimposed on internal tides. In this marginal sea, the cumulated effects of these dynamical constraints result in water mass transformation as observed by in situ observations. The objective of this paper is to document the M2 internal tides in the Solomon Sea and their impacts based on two regional simulations with and without tides. Because the Solomon Sea is under the influence of ENSO, the characteristics of the internal tides are analyzed for two contrasted ENSO conditions: the 1997-1998 El Niño and the 1999 La Niña. The generation, propagation and dissipation of the internal tides are sensitive to changes in stratification and mesoscale activity between El Niño and La Niña. Mode 1 is the dominant mode to propagate baroclinic tidal energy within the Solomon Sea, but the El Niño conditions, with stratification closer to the surface, are favorable for the propagation of mode 2. The la Niña case with a high level of mesoscale activity favors the appearance of incoherent internal tides. These results illustrate the complexity in predicting internal tides in order to access meso and submesoscale signatures from altimetric missions, including the future SWOT mission. Diapycnal mixing induced by the internal tides is efficient in eroding the salinity maximum of the upper thermocline water, and in cooling the surface temperature interacting with the atmosphere. Such effects are particularly visible far from the strong currents, where particles may experience the tidal effects during a longer time. Nevertheless, the impacts are different when considering particular ENSO conditions. The interaction of internal tides with the surface mesoscale activity reduces surface cooling during El Niño 1998, but increases surface warming during La Niña 1999, with possible impacts on regional air sea interaction.

1. Introduction

The Solomon Sea is a marginal sea that is the last passageway for the low-latitude western boundary currents (LLWBCs) of the Southwest Pacific that connect the subtropics to the equator by supplying water of subtropical origin to the Equatorial Undercurrent (EUC), Warm Pool, and Indonesian Throughflow (Tsushiya, 1989; Grenier et al., 2011). It is an important place for tropical circulation and climate that motivates the CLIVAR Southwest Pacific Ocean Circulation and Climate Experiment (SPICE) program (Ganachaud et al., 2014). Marginal seas have long been identified as regions that contribute significantly to kinetic energy dissipation and water mass modification (Munk and Wunsch, 1998; Price and Yang, 1998; Egbert and Ray, 2000). Their topographic properties make them unique regions where water properties are transformed by lateral stirring and vertical mixing due to a mixed of energetic eddy field, and tidally driven internal wavefield. An abundant literature exists on the South China Sea and the Indonesian Seas, illustrating this distinctive feature of marginal seas, but not in the Solomon Sea, even though the Southwest Pacific and in particular the Solomon Archipelago are recognized as areas of generation of energetic internal tides (Niwa and Hibiwa, 2001). Internal tides have been observed at 2°S-156°E from a TOPEX/Poseidon crossover and a Tropical Atmosphere-Ocean (TAO) mooring, propagating northeastward from the Solomon Islands (Gourdeau et al., 1998).

The Solomon Sea is bordered by the main island of Papua New Guinea (PNG) to the West, the PNG islands of New Britain (NB) and New Ireland (NI) to the North, and the Solomon Islands to the East (Fig. 1). The circulation in this semi enclosed basin is highly constrained by such bathymetric features, and has been described in numerous recent studies, from observations (Cravatte et al., 2011; Hristova and

https://doi.org/10.5194/os-2019-94
Preprint. Discussion started: 26 September 2019

Ocean Science Discussions

Kessler, 2012; Davis et al., 2012; Gasparin et al., 2012), and model outputs (Melet et al., 2010; Djath et al., 2014). A strong Low Latitude Boundary Current (LLWBC) , the New Guinea Coastal Undercurrent (NGCU) fed by the Gulf of Papoua Current (GPC) and the North Vanuatu Jet (NVJ), flows from the southern entrance of the Solomon Sea along the PNG coast. When approaching the New Britain coast, it separates into two branches that exit the Solomon Sea through Vitiaz and Solomon Straits. The NGCU flows at the thermocline level below highly variable surface currents including the New Guinea Coastal Current (NGCC), and the Solomon Strait Inflow (SSI) that is the part of the South Equatorial Current (SEC) entering the Solomon Sea through Solomon Strait. Instabilities of these large-scale currents generate large mesoscale eddies that account for most of the surface eddy kinetic energy (EKE) (Gourdeau et al, 2014, 2017; Hristrova et al. (2014), and interaction of the mesoscale flow with topographic features generate submesoscale eddies and fronts (Srinivasan et al., 2017).

Specific water masses entering the Solomon Sea are the South Pacific tropical Water (SPTW, $\sigma_\theta \sim 24.5$) in the upper thermocline level (UTW, $23.3<\sigma_\theta<25.7$), referred to as the upper salinity maximum water, and the Antarctic Intermediate Water (AAIW, $\sigma_\theta \sim 27.2$) in the intermediate water range (IW, $26.7<\sigma_\theta<27.5$) identified by a salinity minimum. These water masses undergo significant modifications along their pathways through the Solomon Sea, characterized by a cooling and freshening of the SPTW, and a warming and an increase in salinity of the AAIW mainly due to diapycnal mixing (Fig. 3 in Germineaud et al., 2016; Melet et al., 2011). The modification of UTW affects the western Pacific with potential downstream effects on the eastern Pacific when the EUC upwells in the tropical eastern Pacific Ocean (Tsuchiya et al., 1989; Fine et al., 1994; Grenier et al., 2011; Qin et al., 2016).

In the Solomon Sea, thorpe scales and finescale methods were used on in situ observations to indirectly estimate the rate of dissipation of kinetic energy (Alberty et al., 2017). Depth-mean energy dissipation in the Solomon Sea is elevated by a factor of eight relative to the rest of the equatorial Pacific, and energy dissipation is maximum in the surface and thermocline layers (4.1-23 10^{-8} [W kg^{-1}]). To model water mass mixing in the Solomon Sea, Melet et al. (2011) used the tide based vertical diffusivity parameterization proposed by Koch-Larrouy et al. (2007) for the Indonesian Seas. This parameterization is based on the assumptions that all of the energy of the internal tides within a marginal sea is dissipated within that sea, and that energy dissipation is assumed to be maximum in the thermocline. If their modeled salinity without the parameterization is biased high over the 24.5–27.5 σ_θ range compared to the observed properties, it is biased low with the parameterization, such that the erosion of SPTW is too strong.

The parameterization described above is a first attempt to take into account the effects of internal tides in an ocean model. They are generated at some specific locations where strong tidal currents encounter sharp topography in a stratified ocean. A global view of their generation, propagation, and dissipation has emerged in recent years, mainly from satellite altimetry observations (Dushaw, 2015; Egbert and Ray, 2017; Ray and Zaron, 2016; Zhao et al., 2016, 2018) and global high-resolution numerical models (Arbic et al., 2010; Müller et al., 2012; Shriver et al., 2012; Simmons et al., 2004, Niwa and Hibiwa, 2014). A lot of studies focus on the low mode M2 internal tides, and the Pacific Ocean is particularly investigated because of numerous archipelago are sources of internal tide generation. Numerous regional studies based on insitu/satellite data and regional models have documented internal tides at the Hawaiin ridge (Zaron and Egbert, 2014; Nash et al., 2006; Chavanne et al., 2010; Zhao et al., 2010), at the Indonesian archipelago (Nagai and Hibiya, 2015; Nughoro et al., 2017; Koch Larrouy et al., 2015), at the East China Sea (Niwa and Hibiwa, 2004; Rudnick et al., 2013). No dedicated

https://doi.org/10.5194/os-2019-94
Preprint. Discussion started: 26 September 2019

Ocean Science Discussions Open Access EGU

studies have focused on internal tides in the South West tropical Pacific despite high semi diurnal baroclinic tidal energy (Niwa and Hibiwa, 2011; Shriver et al., 2012). One motivation of this paper is to document internal tides at the Solomon archipelago and their effects on the circulation and water masses in the Solomon Sea based on a regional model with and without tidal forcing.

Satellite altimeter maps show low modes stationary internal tides propagating across basins for thousands of kilometers (Shriver et al., 2012, Zhao et al., 2016, Ray and Zaron, 2016). This picture of internal tides is somewhat partial as shown recently by several authors that point the importance of non stationary tides (Zaron, 2017; Shriver et al., 2014; Buijsman et al., 2017). In the world's oceans up to 44% of the total semidiurnal internal tide signal is incoherent, and in the equatorial Pacific most of the tidal motions are incoherent. Several mechanisms contribute to the incoherence of internal tides. First, the internal tide generation may vary in time due to local changes in stratification (Chavanne et al., 2010; Nash et al., 2012). Second, the propagation of the low-mode internal tides is modulated by spatial and temporal variability in stratification, currents, and vorticity with detectable changes in tidal SSH.

The South West Tropical Pacific is marked by large interannual variability associated with El Niño South Oscillation (ENSO) with LLWBCs that counterbalance the interior geostrophic flow (Melet et al., 2013, Kessler et al., 2019). The Solomon Sea experiences strong interannual variations in relation to ENSO with asymetric circulation between El Niño and La Niña conditions that greatly impact the mesoscale activity, and with temperature and salinity modifications particularly notable for the thermocline water during El Niño conditions (Melet et al., 2013). So, it is suspected that internal tides in the Solomon Sea could be modulated at ENSO timescales with consequences on mixing for water masses flowing through to the equator.

This particular study is a first attempt to investigate and describe internal tides over the complex Solomon Sea and their interaction with the mesoscale-circulation as well as to investigate their potential role on water masses transformation. We will address this issue for two contrasted ENSO periods that exhibits different stratification and mesoscale activity that affect internal tides characteristics. In order to do so, we take advantage of regional simulations at high resolution (1/36°), with and without tidal forcing, that have been performed during a 3 year period including an El Niño and a La Niña event.

The paper is organized as follows. Section 2 describes the regional model of the Solomon Sea with and without tides and the methodology used to analyse the tides. Section 3 describes the contrasted fields between one El Niño and one La Niña events for the model with tides. Section 4 describes the generation, propagation and dissipation of the M2 baroclinic tide during the two ENSO conditions with a focus on their vertical signatures. Section 5 describes water mass transformation due to the tides over the complete period of the simulations with and without tides. We illustrate some changes in the surface layer due to tides for the different ENSO conditions. Discussion and conclusion are given in section 6.

2. Data and method

2.1 Model description : NEMO

https://doi.org/10.5194/os-2019-94
Preprint. Discussion started: 26 September 2019

The numerical model of the Solomon Sea used in this study is based on the Nucleus for European Modelling of the Ocean (NEMO) code (Madec, 2008) that resolved the standard primitive equations. It is a 1/36° horizontal resolution model originally developed by Djath et al. (2014). Atmospheric boundary conditions are diagnosed through classical bulk formulae (Large and Yeager, 2009), and wind, atmospheric temperature and humidity are provided from the 3-hourly ERA-Interim reanalysis (Dee et al., 2011). This 1/36° resolution model is embedded into a global NEMO 1/12° ocean model forced with similar atmospheric boundary conditions, and one-way controlled using an open boundary strategy (Treguier et al., 2001). The version used here is discretized on the vertical with 75 levels, and includes the option of realistic tidal forcing. The simulation with tides is forced at the open boundary by prescribing the first nine main tidal harmonics (M2, S2, N2, K2, K1, O1, P1, Q1, M4) as defined from the global tidal atlas FES2014 (Carrere et al., 2018) through a forced gravity wave radiation condition. More technical details on this configuration may be found in Tchilibou et al. (2018).

Two simulations are performed: one without tidal forcing (R36), and one with tidal forcing (R36T) over the 1997–1999 period. Daily mean model outputs are saved as R36(T)d, as well as instantaneous fields saved hourly (R36(T)h) to document the baroclinic tides during two 3-month periods: from January–March 1998, and from April-June 1999. The former period corresponds with an El Niño period, and the latter with a La Niña period. These two periods in R36Th offer extremes in local stratification conditions, with a possible impact on the internal tides. The longer series of R36d and R36Td will be useful to investigate the effects of high frequency baroclinic tides on the Solomon Sea circulation and its water masses. These simulations have been already used by Tchilibou et al. (2018) to illustrate the internal tides as the main source of discrepancy between modelled (without tides) and altimetric sea surface height wavenumber spectra.

2.2 Tides decomposition and energetics

a) Barotropic/baroclinic tides decomposition

The central issue here is the separation of barotropic and baroclinic components, in terms of velocity and pressure as discussed in Nugroho et al. (2017). Although intuitive, this issue is not trivial and we need to define precisely the meaning of "barotropic" and "baroclinic" dynamical terms. The method used to separate surface and internal tides ultimately defines properties such as internal tide generation and the depth structure of the internal tide energy flux (Kelly et al., 2010).

The most common definitions can be summarized as follow:

1, barotropic tides are the ones that would be present in the absence of ocean stratification (uniform density ocean), and baroclinic tides are the departure from those barotropic tides when stratification is taken into account. This definition has been widely adopted by many authors. However, barotropic tides in a non-stratified ocean will differ significantly from barotropic tides in a stratified ocean. As a consequence, the "baroclinic" tides obtained by differencing non-stratified ocean tides and stratified ocean tides will contain parasite barotropic residuals.

2, barotropic tides are the depth-averaged part of the tidal dynamics in a stratified ocean, baroclinic tides being then the residual between the full 3D tides and the barotropic tides. This definition is quite conventional and popular, and mostly acceptable for first order analysis. This reflects the idea that

https://doi.org/10.5194/os-2019-94
Preprint. Discussion started: 26 September 2019

baroclinic quantities vanish when integrated with depth (also called the baroclinicity condition). This method has some consistency with model modes under a rigid lid assumption, but in the free surface case, it doesn't take account of the surface pressure, leading to an unsatisfactory tidal energy budget. The surface tide pressure can be expressed as the depth average of total pressure plus a new depth-dependent profile of pressure, which is due to isopycnal heaving by free surface movements (Kelly et al., 2010).

3, barotropic tides are the fast mode in a Sturm-Liouville vertical mode theory framework, and baroclinic tides are the slow modes. By using modal decomposition, this technique solves the inconsistencies that come from surface pressure due to isopycnal displacement. This decomposition applied on idealized cases also gives a barotropic energy flux that is consistent with energy conversion, and has good agreement with observations (Kelly, 2012). This definition has a much better physical meaning, and has attracted much attention in the tidal community. It has been applied on models with realistic forcing and complex bottom topography such as in the Indonesian seas (e.g., Nugroho et al., 2017).

In this study, we use this vertical mode decomposition to define and separate the barotropic and baroclinic tides. In practice, the vertical mode computation and the simulation's decomposition have been performed by solving the generalized Sturm-Liouville eigenvector/eigenvalue problem. Each successive mode decreases in group speed (c0 >c1 >c2 >…) and increases in horizontal wavenumber (k0 <k1 <k2 <…). The lowest-mode tide (n = 0) is the surface barotropic tide, and the higher-mode tides (n ≥ 1) make up the internal tides with n zero crossings on the vertical for horizontal velocities.

b) Energy budget : Generation, propagation and dissipation

The generation, propagation, and dissipation of the barotropic and baroclinic tide is investigated with the time-averaged and depth-integrated barotropic and baroclinic energy equation (Niwa and Hibiya, 2004; Carter et al., 2008; Nagai and Hibiwa, 2015, Simmons et al., 2004; Buijsman et al., 2014, Nughoro et al. 2017]. In each barotropic and baroclinic equation, the depth-integrated energy is partitioned into tendency, flux divergence, non-linear advection, barotropic to baroclinic conversion, and dissipation. We can ignore the rate of change term as the period of averaging (month and year) makes this term orders of magnitude smaller than the other terms in equations (1 & 2). Similarly, the internal-tide self-advection is also small (Simmons et al., 2004; Buijsman et al., 2014). The non-linear advection terms are assumed to be small in both the barotropic and baroclinic equations. This means that little energy is transferred between tidal harmonics. The equations resume to:

$$\nabla.\mathrm{Fbt} + \mathrm{Dbt} + \mathrm{C} = 0 \quad (1)$$

$$\nabla.\mathrm{Fbc} + \mathrm{Dbc} - \mathrm{C} = 0 \quad (2)$$

Where bt indicates the barotropic term and bc indicates the baroclinic terms, F=(Fx;Fy) are the fluxes in the x(east-west) and y(north-south) directions, D is dissipation, and C is the barotropic to baroclinic energy conversion. D is computed as the residual of the flux divergence and conversion terms. The conversion term is identical in the barotropic and baroclinic equations; and it appears as a sink in the barotropic equation and a source in the baroclinic equation. It is defined as in Nughoro et al. (2017):

$$C = (\bar{u}p')_{z=-h}\,\nabla_h d$$

https://doi.org/10.5194/os-2019-94
Preprint. Discussion started: 26 September 2019

Where p' is the perturbation pressure, $\bar{u}$ is the M2 harmonic fit for the barotropic velocity, h the bottom depth, and d is the total depth (d=h+η, η the surface elevation).

The propagation of barotropic and baroclinic tides are examined through the divergences of the barotropic (Fbt) and baroclinic (Fbc) energy flux, respectively, and defined as in Nughoro et al. (2017):

$$Div(Fbt) = \int_d^\eta \nabla_h \, \overline{up}$$

$$Div(Fbc) = \int_d^\eta \nabla_h \, u'p'$$

The overbar sign is for barotropic velocity (u) and pressure (p), and u', p' is the velocity perturbation and pressure perturbation, respectively.

c) Calculating (non) phase-locked internal tides

For each 3-month period of hourly time series corresponding to the 1998 El Niño and the 1999 La Niña, the simulated time series are first harmonically analyzed to obtain the amplitude and phase of the main diurnal (K1, O1, P1) and semidiurnal (M2, K2, S2, N2) components. Then linear tidal frequency motions of vertical displacement and horizontal velocity are projected onto the barotropic and nine first orthogonal vertical modes (n =0, 1, 2, …,9). This provides the description of the barotropic tide (mode 0) and the phase-locked baroclinic tide that can be analyzed by each mode or as the sum of the 9 baroclinic modes. These harmonic analyses provide only the tidal signal that is coherent with the astronomical forcing over each 3-month period. But several mechanisms can contribute to incoherent tides such as changes in stratification, interactions with the mesoscale flows and the internal wave field (Buijsman et al., 2017). A proxy for the incoherent part of the internal tides is to filter the signal for periods < 24 hr once the stationary, phase-locked tides have been subtracted. This incoherent or non-phase-locked component also includes the internal wave field and very rapid ocean circulation, but the variance of the corresponding SSH field in the simulation without tides is small enough (Tchilibou et al., 2018; their Fig. 9) that it is mainly a tidal signal in the simulation with tides.

3. Contrasted El Niño/La Niña conditions

In addition to the model description and its validation, this section is motivated by a presentation of the Solomon Sea circulation, its variability, and its vertical stratification for two distinct ENSO periods: the 1998 El Niño and the 1999 La Niña. All of these dynamical elements may influence the internal tide fields from its generation to its propagation and dissipation.

3.1 Circulation and EKE

The interannual variability of the surface circulation in R36Td is consistent with previous studies on ENSO cycles (Hristova and Kessler, 2011; Melet et al., 2013) (Fig. 2). At ENSO timescales, the LLWBCs transport tends to counterbalance the interior geostrophic transport. During the 1998 El Niño period, the NGCC/NGCU intensifies and increases the transport towards the equator to counterbalance the equatorial discharge (Fig. 2a). During the 1999 La Niña period, the strengthening of the trade winds increases the SEC intensity in the equatorial band, and the inflow transport at Solomon strait. The induced circulation anomalies in the Solomon Sea are not symmetric between the two ENSO states because of a bathymetric control at Vitiaz Strait which plays a stronger role during El Niño when the

https://doi.org/10.5194/os-2019-94
Preprint. Discussion started: 26 September 2019

Ocean Science
Discussions
Open Access

NGCC intensifies and because of an additional inflow through Solomon Strait during La Niña when the NGCC weakens (Melet et al., 2013).

A consequence of this asymmetry is a level of surface Eddy Kinetic Energy (EKE) that varies strongly between the two ENSO states, as shown on the mean EKE maps representative of the different periods (Fig**. 2**). During El Niño state, despite the increase in LLWBC transport, the flow is relatively laminar with a low level of EKE. However during La Niña state, the strong shear between the NGCC and the SSI is at the origin of a high level of EKE as described in Gourdeau et al. (2014). Therefore, the mean circulation and the level of intraseasonal EKE of these two contrasted periods provide different background conditions for interactions between currents and internal tides**.**

3.2 SSH variability

SSH variability, as measured by altimetry, is a good proxy of energetic motions. In the tropics, the SSH wavenumber spectral signature of mesoscale variability is highly impacted by the signature of internal tides for scales up to 250-300 km (Tchilibou et al., 2018). This complicates the analysis of these spatial scales with a mix of mesoscale dynamics and internal tides, for all altimetric observations and in the context of the future SWOT mission. This new swath-altimetry mission will be a great opportunity to study the 2D interactions between both dynamics in the tropics. The objective of this subsection is to give some insight on the SSH variability associated with mesoscale activity and internal tides in the Solomon Sea.

The largest SSH variability in the Solomon Sea is at seasonal and interannual time scales in response to large-scale and low-frequency atmospheric forcing, and is responsible for up to 80% of the gridded AVISO altimetric signal variance (Melet et al., 2010b; Gourdeau et al., 2014). These longer time scales have an EKE level reaching 2000 cm^2/s^2 that is of same order as the intraseasonal EKE level during a La Niña period, as shown above from the R36Th simulation.

The SSH variability associated with the intraseasonal EKE described above is a mix of mesoscale variability down to sub-inertial frequencies, and internal waves at super-inertial frequencies (Savage et al., 2017). The super-inertial frequency range corresponds mostly to internal tides signatures as confirmed by the quasi null SSH variability in the simulation without tides for such frequency range (not shown). Figure 3 shows how the SSH standard deviation of the R36Th outputs changes between the El Niño and La Niña periods for the full signal, the mesoscale component (> 48 hr), and the internal tides component (< 48 hr). The variability of the incoherent part of the internal tides discussed in the next section is also plotted.

Outside the Solomon Sea, the patterns of SSH variability are similar between the two ENSO states, although there us more mesoscale energy during El Nino (Fig. 3a,b). Increased variability is associated with instabilities of the GPC when it turns eastward at PNG coast near 12°S, 148°E, and with instability from the SECC-SEC current system east of the Solomon Islands near 8°S, 164°E (Qiu and Chen, 2004). Inside the Solomon Sea, the patterns of SSH variability differ greatly between the two ENSO states by a factor of 2-3. The El Niño period is marked by low variability with small scale structures, compared to the La Niña period where high variability occupies the central Solomon Sea, in accordance with the EKE signal (Fig**. 2**). During the El Niño period, the level of mesoscale variability is of the same order of magnitude as the internal tides (Fig. 3c,e). This explains why the full signal is composed of small structures mixing both mesoscale activity and internal tides. The most energetic internal tides signal is

https://doi.org/10.5194/os-2019-94
Preprint. Discussion started: 26 September 2019

concentrated in the Solomon Sea from the southern tip of PNG to Solomon strait (described more in section 4). Incoherent tides have low amplitude, and they are mainly located at Solomon strait. During the La Niña period, the mesoscale variability is largely dominant compared to the internal tides signature (Fig. 3d,f). Note that the patterns of internal tides differ slightly between both ENSO states with a more continuous pattern crossing the Solomon Sea, and a substantial signature of incoherent internal tides in the northern Solomon Sea during La Niña. This suggests possible interaction between mesoscale dynamics and internal tides, with a possible effect on changes in water mass stratification depending on the ENSO phase. This will be explored more in section 4.

3.3 Water masses and Stratification

Internal tides are sensitive to ocean stratification and such stratification is susceptible to be modified at ENSO time scales because of temperature and salinity anomalies of the different water masses entering the Solomon Sea (Melet et al., 2013). Because the internal tide propagates meridionally across the central Solomon (e.g. section 4), the section at 154°S is used to investigate and validate the water mass characteristics, and to illustrate the corresponding stratification changes in different ENSO conditions.

First, the averaged salinity section from R36Td is compared with that of the CARS climatology (www.cmar.csiro.au/cars) (Fig. 4a, b). According to CARS, we find the maximum salinity of the SPTW waters (σ_θ=24.5, z~150 m), and the minimum of salt of the AAIW waters (z~800m) (e.g. section 1).

To illustrate the changes in the properties of water masses with the ENSO cycle, salinity anomalies for El Niño and La Niña periods from R36Td are calculated with reference to the complete period (Fig. 4c, d). Main changes in salinity concern the first 500 m below the surface, and particularly the upper thermocline water ($23.3<\sigma_\theta<25.7$). These interannual salinity anomalies mainly reflect large scale variability due to the effect of the anomalous wind stress curl that develops at ENSO timescales in the area by strongly pulling up (down) the thermocline during El Niño (La Niña), mainly through Rossby waves forced by the anomalous Ekman pumping (Melet et al., 2013).

During El Niño conditions, the resulting thermocline shoaling brings fresher and colder water into the upper thermocline waters compared to neutral ENSO conditions, and saltier/warmer lower thermocline water. The opposite situation prevails during La Niña conditions, with saltier and warmer upper thermocline water, and fresher/colder lower thermocline water. During La Niña conditions, the saltier waters are found not only at upper thermocline levels but also at the surface due to the advection by the strong SSI of central Pacific salty water (Gourdeau et al., 2017).

In consequence of such ENSO variability, the corresponding density sections show a more pronounced thermocline shifted upward during El Niño in comparison with La Niña, particularly in the north of the section (Fig. 4c,d). These density profiles reflect changes in the vertical stratification represented by the Brünt Vaissala frequency (N^2). Figure 5 shows the N^2 profiles characteristic of the 154°E section when averaged in latitude across the Solomon Sea section. Figure 5 compares the CARS climatology with the R36Td simulation characteristic of the mean state, and of the two ENSO phases. First, it is notable that the modelled mean N^2 profile is in good agreement with the CARS climatology with maximum values in the 80-150 m depth range. The ENSO phases are clearly distinguishable from the mean. The La Niña period is marked by a deepening of the maximum N^2 frequency extending the thermocline down to 200 m depth. The situation during El Niño is very contrasted: N^2 is marked by

https://doi.org/10.5194/os-2019-94
Preprint. Discussion started: 26 September 2019

significantly higher values and stronger thermocline gradients, especially in the surface layers with a maximum value at 50 m depth. Internal tides being very sensitive to these N^2 profiles, we can assume that different internal tide characteristics may occur between these two periods.

4. M2 Tides

In this section, the tidal signal simulated by the regional model is described. A first insight into the tides is through temporal spectra. Dynamic height variance frequency spectral density averaged over the Solomon Sea is shown in Figure 6a. Both models with and without tides agree well at low frequency (T > 30 hr). The simulation with tides shows large peaks at diurnal and semidiurnal frequencies, and an energetic supertidal band (T < 12h). The tidal signal is a mixture of barotropic and baroclinic components, and the SSH variance is largely dominated by the former.

The modal decomposition is done for each of the two ENSO phases using R36Th. K1 is the dominant barotropic component within the Solomon Sea (not shown). The first nine baroclinic modes that we compute from our model represent more than 90% of the baroclinic energy whatever the ENSO phase. To infer the baroclinic tidal signature ($n \geq 1$) the barotropic tide (n=0, BT) is removed (Tides-BT). The frequency spectra of the Tides-BT SSH signal, averaged over the Solomon Sea, show some differences between the two ENSO phases, especially at M2, S2 frequencies (Fig. 6b, to clearly distinguish their peaks the El Niño spectrum is shifted in period by two hours). This may illustrate the influence of changes in mesoscale activity as well as stratification on internal tide activity. Nevertheless, the main baroclinic tide is at M2 period for both spectra (Fig. 6b). Therefore in the following, our focus will be on the dominant M2 baroclinic component. But a paramount condition is to correctly simulate the barotropic component. First, we assess the barotropic component before we analyze the baroclinic components for the two ENSO conditions.

4.1 M2 Barotropic tide

The realism of the simulated barotropic tides is crucial for the ability of the model to generate realistic internal tides. The barotropic M2 tide simulated by our model is estimated for each of the 3 month ENSO periods, and both estimations provide similar results (not shown). The simulated barotropic M2 tide, forced at the open boundary by FES2014, compares well within the Solomon Sea with the results of FES2014. The M2 barotropic tide is maximum outside the Solomon Sea and almost null within the Solomon Sea (Fig. 7). East of the Solomon Islands, the lines of constant M2 phase **in** Figure 7 illustrate a southward propagation that turns westward at the southern tip of the Solomon Islands with a magnitude that decreases from 30 to 15 cm. The M2 barotropic tide interacts preferentially with bathymetry at Solomon strait (5°-6°S), at the southern extremity of the Solomon Islands and at the southeastern tip of PNG (Fig. 7). The interaction of this barotropic tide with the topography enclosing the Solomon Sea is favorable for generating internal tides.

4.2 M2 baroclinic tide

Following the method described in section 2.2c, we access only the coherent part of the internal tides that has the advantage to be predictable, and so provides a correction for altimetric measurements. Here we describe this M2 phase-locked internal tide.

a) SSH validation of the phase-locked component

https://doi.org/10.5194/os-2019-94
Preprint. Discussion started: 26 September 2019

An estimate of the M2 stationnary or phase-locked baroclinic tide based on more than 20 years of altimeter measurements is given in Ray and Zaron (2016). Their result is shown in Figure 8a. The altimetric M2 baroclinic tide has a strong amplitude in the Solomon Sea from the Solomon strait in the north to the eastern tip of PNG. The amplitude of the baroclinic (coherent) tide is on the order of 3-5 cm in the Solomon Sea with an approximate wavelength of 150 km. The M2 internal tide estimated by the model during the 3-month La Niña period (Fig. 8b) is consistent with that estimated from the 20 years of altimetry, but with higher amplitudes at Solomon strait. The M2 internal tide estimated during the El Niño period has shorter wavelengths and more dispersion over the entire domain of the Solomon Sea. Both patterns of the M2 coherent baroclinic tide resemble the full signal of internal tides calculated over these 3-month periods (Fig. 3), illustrating that M2 is the main contributor to the internal tide variability. Indeed, the semi diurnal tide corresponds to more than 70% of the full internal tide variance within the Solomon Sea.

The large internal tide differences between the two ENSO states raise the question of the predictability of the stationary internal tide when the level of mesoscale activity and the stratification change at interannual time scale. Note that it is during the La Niña condition when the mesoscale activity is high (e.g. Fig. 3) that the M2 internal tide appears well organized in accordance with the altimetric estimation. One explanation is the deeper stratification during La Niña than during El Niño (e.g. Fig. 5). This means that the M2 baroclinic tide is more sensitive to the stable baroclinic mode 1 during La Niña whereas it is more sensitive to higher dissipative modes during El Niño. It also explains why the coherent baroclinic M2 tide of Ray and Zaron (2016), particularly noticeable to mode 1, looks like the modeled results for the La Niña period.

Mesoscale activity influences also the characteristics of baroclinic tides. Indeed, the part of coherent baroclinic tides versus the incoherent part varies drastically between the two ENSO states. During El Niño, when the LLWBCs are strong and the flow relatively laminar, the coherent baroclinic tides explains 67% of the variance of the full internal tides, and only 50% during La Niña when mesoscale is strongly active. This is clearly shown on the maps of incoherent baroclinic tides (Fig. 3) where strong incoherent baroclinic tides are present in the northern Solomon Sea basin during the La Niña period.

b) Generation, propagation and dissipation

The distribution of the baroclinic energy flux, the energy conversion rate, the divergence of the baroclinic energy flux, and the baroclinic energy dissipation calculated for the La Niña and El Niño periods are all shown in Figure 9 for the M2 harmonic. Table 1 also provides the area integrals of the different terms of the energy equation: the divergence of the barotropic/baroclinic flux (Div(FBT)/Div(FBC)), the dissipation of barotropic/baroclinic flux (DBT/DBC) and the conversion rate from barotropic to baroclinic energy (CVR) (e.g. section 2.2); these are quantified for the different ENSO phases at the different generation sites as defined by the boxes on Fig. 9f.

For both ENSO phases, the M2 barotropic energy flux is coming from the Equatorial Pacific and flows southward in the southwestern pacific, east of Solomon Island and turns westward south of the Solomon Sea. There are two main ways for the M2 tide to enter the Solomon Sea either by the Solomon Strait or by the southern portal. On its way it encounters three main complex bathymetric features that generate intense internal tides: the Solomon strait (5°-6°S), the southern extremity of the Solomon Islands and the southeastern tip of PNG. They are the three main areas of baroclinic tide generation as shown by the negative values of the energy conversion rate (the sign is consistent with

https://doi.org/10.5194/os-2019-94
Preprint. Discussion started: 26 September 2019

it being a sink term in the barotropic equation) (Fig. 9a,b). Weaker internal tides are also found within the Solomon Sea on the seamounts extending eastward from the Woodlark archipelago (~9°S - 155°E).

Strong baroclinic energy fluxes originate in regions where significant energy conversion is identified (Fig. 9c,d). The excited baroclinic energy radiates away from the generation zones, and the largest fluxes are contained within two beams: one propagating inside the Solomon Sea and the other one propagating in the open ocean. The main baroclinic energy flow entering the Solomon Sea comes from the southeastern tip of PNG where it propagates to the northwest, and from the Solomon Strait where it propagates to the southwest. Both fluxes cross the Solomon Sea between 153°E and 156°E. This description is in accordance with the SSH signature of the M2 baroclinic tide (Fig. 8).

Estimates for dissipation of internal tides (Fig. 9e,f**)** in the model are made as a residual between the divergence of the baroclinic flux (Fig. 9c,d) and the conversion rate (Fig. 9a,b**)** following equation (2). This equation does not take into account the non-linear advection (Buijsman et al. 2016) that might be contained in the dissipation estimate. This might overemphasize the energy of the dissipation estimate. It is interesting to note that most of the dissipation occurs near the generation sites. We note, however, a non-zero dissipation along the pathways of internal tides, especially those in the northern Solomon Sea.

Some modulations exist between the El Niño and La Niña periods, with a slightly stronger conversion rate, stronger local dissipation and stronger energy flux during the El Niño period. The dissipation is also quite significant during La Niña in the northern Solomon Sea, away from the generation site (Figure 9, Table 1).

c) Quantification of the Energy budget for the two ENSO states

For the Solomon strait box (Fig. 9f, red), the divergence of the barotropic flux energy is around 3 GW (Table 1). The majority of this flux divergence is converted into baroclinic tides (~ 70%, ~ 2.10 GW) with the bottom friction (barotropic dissipation) accounting for ~ 0.85 GW. The majority of the energy converted from barotropic to baroclinic energy is dissipated within the box, but there is stronger local dissipation during El Niño (75%) than during La Niña (66%). So we observe a stronger baroclinic energy flux radiating out of the box during La Niña period that may dissipate in the far field. 0.7 GW radiates out of the box as baroclinic flux during La Niña against 0.55 GW during El Niño. More than half of this energy propagates into the Solomon Sea.

For the box representative of the southern extremity of the Solomon archipelago (Fig. 9f, green), the divergence of the barotropic flux energy is around 6 GW, twice that of the Solomon strait box. The majority (~ 60%) of this flux divergence is converted into baroclinic tides (4 GW) with the bottom friction (barotropic dissipation) accounting for 2 GW. The majority of the energy converted from barotropic to baroclinic energy is dissipated within the box and the dissipation rate varies from 70% to 80% between El Niño and La Niña, respectively. During the El Niño event, the barotropic flux divergence is larger than during the La Niña event (6.83 vs 5.89 GW). In consequence the conversion rate is stronger in the same proportion (Table 1), but, the dissipation is identical between the two ENSO events (~3GW). The baroclinic flux radiating out of the box doubles during El Niño (1.27 GW against 0.75 GW strait during La Niña) meaning that more dissipation must occur in the far field during El Niño. Most of this baroclinic energy radiates out of the Solomon Sea, and only 0.24/0.17 GW radiates into in the Solomon Sea during the El Niño/La Niña periods.

https://doi.org/10.5194/os-2019-94
Preprint. Discussion started: 26 September 2019

The PNG box (Fig. 9f, blue) is smaller than the other boxes, and the divergence of the barotropic flux energy is around 1.8 GW. More than 75% of this flux divergence is converted into baroclinic tides (1.36 GW). In contrast to the other boxes, the majority of the energy converted from barotropic to baroclinic energy radiates out of the box (0.75 GW), and 0.22 GW radiates into the Solomon Sea. No contrasted situations are observed between the two ENSO phases in this area crossed by the strong NGCU.

In summary, there are three areas where a large part of the barotropic flux energy is converted into baroclinic energy (63 to 79%), and a considerable fraction of the excited baroclinic energy is dissipated locally (46 to 80%). The two main generation sites radiating baroclinic tidal energy into the Solomon Sea are at Solomon strait and at the Southeast extremity of PNG. The generation box at Solomon strait radiates most of the baroclinic energy, especially during the La Niña state with a 27% increase of the energy flux compared to El Niño. There is a strong modification of the circulation at this site between the two periods, since the strong northward LLWBC current exiting the Solomon Sea during El Niño is replaced by the southward SSI current during the La Niña period that favors the advection of the tidal baroclinic energy inside the Solomon Sea. Most of this baroclinic energy is dissipated in the northern Solomon Sea as illustrated by Figure 9f, showing higher dissipation in the northern Solomon Sea during La Niña compared to El Niño. Indeed, the higher EKE level during La Niña than during El Niño (Fig. 2) favors stronger interactions between eddies and internal tides. This appears to render the internal tide more incoherent (e.g. Fig. 3gh) and to increase the tidal dissipation. The impact of ENSO is particularly visible at the southern Solomon Sea with a 70% increase of the baroclinic flux radiating away from this generation site during El Niño compared to the La Niña period. The EKE is strongest in this area during La Niña with higher dissipation and in consequence, there is a lower baroclinic energy flux radiating away.

d) Vertical signature

In the previous sections, baroclinic tides were investigated by considering their depth-integrated form. For a more quantitative discussion on the vertical structure of the propagating M2 baroclinic tide, we perform modal decomposition of the model-predicted baroclinic energy fluxes. Figure 10 shows the spatial distribution of the M2 modes 1 and 2 for the El Niño and La Niña states. These two modes account for almost the entire variance of the full baroclinic M2 energy flux. Mode 1 is largely the dominant mode (note the different scales between mode 1 and 2). However, Mode 2 is particularly present within the Solomon Sea during the El Niño period compared to the La Niña period where Mode 2 energy is locally dissipated at the generation sites. One explanation for such a difference is the change in stratification between the two ENSO states, with stratification closer to the surface during El Niño that favors the excitation of higher order modes (Fig. 5). Whatever the ENSO state, Mode 1 energy flux propagates into the Solomon Sea, from Solomon strait and from the southeastern tip of PNG. The PNG flux is relatively stable (see Table 1) and follows the NGCU pathway until the Woodlark Archipelago (9°S). Whereas the Solomon strait flux exhibits strong changes in propagation between the two ENSO states that appear related to the background circulation. During El Niño, this flux is directed to the South West in the lee of the LLWBC exiting at Solomon strait. It breaks into two branches when encountering the northward NGCC to the West. During La Niña, the flux is southward in the wake of the Solomon strait inflow. This suggests the constraint of the propagation of the baroclinic tidal energy by the background circulation. The mode 1 baroclinic flux emanating from the south Solomon Sea is less intense during La Niña (Table 1) and this flux exits the Solomon Sea to the South.

https://doi.org/10.5194/os-2019-94
Preprint. Discussion started: 26 September 2019

Ocean Science Discussions
Open Access
EGU

To illustrate these changes brought by the stratification and the circulation on the vertical structure of the M2 baroclinic flux, we show the meridional baroclinic energy fluxes for the two ENSO phases along the section at 154°E which transects the prominent baroclinic energy flux in the Solomon Sea (Fig. 11). The highest energy fluxes are located in the upper 300 m depth but they extend deeper during the La Niña period than during El Niño in accordance with changes in stratification (Fig. 5). During El Niño, when the NGCC/NGCU are strong, the northward baroclinic energy flux from the southern tip of PNG crossed practically all the Solomon Sea up to 6.5°S. During La Niña, when the SSI is strong, the baroclinic energy flux from the Solomon Strait extends to the south and the southward and northward fluxes meet in the central Solomon Sea (8°S).

In summary, the M2 baroclinic energy flux is concentrated in the first 200-300m depth Propagation, and depth penetration of this energy vary between the two ENSO states depending on the background circulation and stratification. Mode 1 accounts for most of the propagation of the energy flux but Mode 2 is also significant, particularly during the El Niño period characterized by a stratification close to the surface.

5. Internal tides and water mass transformation

As discussed in the introduction, the Solomon Sea is an area of strong water mass transformation between the southern entrance of water masses and their exit at the different northern straits. This strong modification has been illustrated by Germineaud et al. (2016) in their analysis of Solomon Sea water masses from in situ observations, based on two dedicated cruises. Most of the transformation is on the SW, UTW, and IW water masses (their Fig. 3). The salinity maximum of the SPTW waters in UTW is the key variable regarding the impact of T–S modifications on the EUC. Whereas SW, which enter into the Pacific warm pool, are particularly relevant in modifying the air-sea interaction there. At depth, the IW influence the water mass properties of the cross-equatorial intrusion, in turn impacting on the North and equatorial Pacific's overturning circulation (Qu and Lindstrom, 2004). In the following, the discussion focuses on these three water masses of interest. As shown in the previous section, interactions of barotropic tides with the topography give rise to strong internal tide generation and tidal energy dissipation in the Solomon Sea. These processes, combined with the large eddy activity associated with boundary currents and their recirculation, may lead to enhanced mixing and contribute to the erosion of the T–S characteristics of the thermocline water (TW).

Here, we take advantage of our twin, forced with and without explicit tides, to analyze the impact of internal tides on the Solomon Sea's water mass modification. If the preceding section described the characteristics of internal tides based on short 3-month periods of hourly outputs, this section addresses the longer term impacts of internal tides on the Solomon Sea water masses, based on daily outputs from the three year simulations with tides (TIDE) and without tides (NOTIDE). The 3 year time series is just long enough compared to the transit time of the particles transiting through the Solomon Sea that vary from 40 to 370 days following the water masses of interest for this study (Melet et al., 2011). We will close this section by considering the Surface Water (SW, $\sigma<23.3$) changes during the different ENSO conditions.

a) Longer term changes between TIDE and NOTIDE simulations

We have analyzed the mean temperature and salinity changes induced by adding the tidal forcing to our regional models, for the three key water masses of interest: SW (σ <23.3); UTW (23.3<σ<25.7) and IW (26.7<σ<27.5). At first order, comparison of both simulations shows that tidal mixing induces fresher UTW and saltier SW and IW, and changes are particularly notable in the Solomon Sea (Fig. 12). It means that the SPTW salinity maximum is eroded, and the corresponding salt flux is transferred downward to IW, and upward to SW. In the same way, the diapycnal mixing from tides at the thermocline level induces a heat flux that cools the ITW and SW, and warms the IW. This results in a weaker stratification at the thermocline level in the TIDE simulation compared to the NOTIDE simulation (e.g. Fig. 5).

The spatial distribution of the anomalies shows that the highest anomalies are observed in the eastern Solomon Sea along the Solomon archipelago with fresher salinity up to -0.08 psu in the UTW and saltier salinity up to 0.08 psu in the surface waters (SW). It corroborates the fact that most of the tidal baroclinic energy is dissipated locally when generated at the Solomon Islands as shown by the energy balance at the two main boxes of internal tide generation (Table 1) whereas at the PNG box, most of the tidal baroclinic energy propagates with the LLWBC.

Focusing on the UTW, the NOTIDE simulation clearly shows the intrusion of the high salinity SPTW water advected by the NVJ in the Solomon Sea (Fig. 13a). It occupies a large part of the Solomon Sea when propagating northward with the NGCU. It is mainly eroded in the southern part of the Solomon Sea with a 0.06 freshening. Interactions between the NGCU and the bathymetry are suspected to play a major role to erode the salinity maximum. The TIDE simulation shows an extension of the salinity maximum limited to the NGCU pathway, and it is eroded all along its route, especially in the northern Solomon Sea (Fig. 13b). This suggests that diapycnal mixing is particularly efficient in the eastern and northern basin (Fig. 12d). One explanation for this tidal mixing being particularly efficient in the eastern Solomon Sea is its location far from the LLWBC route with a longer transit time of particles in this region favorable to tidal mixing.

The TIDE simulation shows a strong east-west contrast between the salinity signature driven by the LLWBCs and the lower salinity along the Solomon archipelago. This contrast is also visible in the CARS climatology, although a fresher bias of about 0.02 psu may be noted in the TIDE simulation compared to CARS (Fig. 13c). This east-west contrast is also visible in Melet et al. (2011, their Fig. 4) when using a model including the tidal parameterization, but with a stronger freshening of 0.1-0.2 psu. Although the lowest UTW salinity along the Solomon archipelago is in good agreement between CARS and the TIDE simulation, the highest UTW salinity exhibits a fresh bias compared to CARS that exists in the NOTIDE simulation and is accentuated in the TIDE simulation. Outside the Solomon Sea, the large salinity bias in the Bismark Sea (North of New Britain), and in the Gulf of Papua in the NOTIDE simulation compared to CARS has been slightly reduced in the TIDE simulation.

This comparison with the long-term CARS climatology has some limitations with regard to the particular conditions of our 3 year simulation including an El Niño and a La Niña event. An illustration is the salinity maximum at the latitude of Solomon strait in CARS (5°S, Fig. 13c) that extends outside the Solomon Seas into the surrounding open ocean. It doesn't match our 3-year period simulations, where this salinity maximum in the open ocean is shifted to the south (Fig. 13a,b). When using salinity data from the monthly interannual CORA05 product based largely on Argo data (Cabanes et al., 2013) and averaged over the same period as our simulations, this southward shift is also observed (not

https://doi.org/10.5194/os-2019-94
Preprint. Discussion started: 26 September 2019

shown). (We note that the CORA05 database has few observations inside the Solomon Sea, which is the main interest of our comparisons).

b) Impact of tides at the surface

At the surface, the cooling of SW by the tides affects the SST field that in return affects the latent heat flux and the corresponding net heat flux (Qnet). This corresponds to a positive Qnet anomaly between the simulation with and without tides (not shown) that acts to reduce the SST cooling induced by internal tides. Averaged over the Solomon Sea, the SST cooling due to the tides is of -0.09°C at 30 m depth, and only -0.05°C at the surface. Nevertheless, it could be of importance with regard to air-sea coupling, as noted for the Indonesian Seas by Koch-Larrouy et al. (2010).

The transit time of particles in SW being less than 3 months (Melet et al., 2011) allows us to investigate how different ENSO states impact on the SST analyses. Although the 3-year mean effect of the tide is to cool the SST, the differences between the TIDE and NOTIDE simulations for the two ENSO periods show contrasting situations. Figure 14 shows that during the El Niño period, both simulations with and without tides are characterized by negative temperature anomalies at 30 m depth compared to the 2-year mean fields, but the extra tidal mixing tends to reduce these negative temperature anomalies (leading to a positive difference; bottom panel). During El Niño, the averaged SST difference between the TIDES and NOTIDES simulations is only 0.04°C but can reach 0.5°C along the LLWBC pathway (Fig. 14e). In contrast, the La Niña period has large positive temperature anomalies at 30 m depth compared to the mean in both simulations, but this SST warming is not diminished but is increased by the inclusion of tides (a difference of 0.3°C averaged over the Solomon Seas, Fig. 14f). During La Niña, the tides are mixing up the deeper warmer anomalies into the surface layer in the northern Solomon Sea (Figs 4d, 5), and at the same time, the southward baroclinic tidal energy flux (Fig. 9c) combined with the southward surface circulation during this 3-month period (Fig. 2b) is bringing more warm surface waters southward through the SSI.

The two upper panels in Figure 14 also highlight how the 3-month averaged EKE varies between the El Niño and La Niña periods, with and without tides. During El Niño when the EKE is already weak (Fig. 2a) and the stratification is shallow (Fig. 5), significant EKE differences occur (Fig. 14e). When averaged over the Solomon Sea, the differences in EKE is -312 cm^2/s^2 between the TIDE and NOTIDE simulations, i.e., around half of the total EKE during this period. The NGCC increases during El Niño, and it is associated in the NOTIDE simulation with a well-marked EKE signature (over the three months period) when the current interacts with the bathymetry at the Southern extremity of PNG and at the Woodlark archipelago. These two locations are important places for internal tide generation, as described in section 4. It is remarkable that such a clear EKE signature disappears in the TIDE simulation, illustrating the interaction and perturbations between the tides and the mesoscale activity. This lower EKE level at these places may explain the higher SST along the NGCC in the TIDE simulation.

During La Niña when the EKE level over the three months period is high (e.g. Fig 2b), interactions between mesoscale activity and tides are also significant with an EKE reduction of -270 cm^2/s^2 between the TIDE and NOTIDE simulations (Fig. 14f). The consequence is a warming of the SST of 0.3°C (averaged over the Solomon Sea) in the TIDE simulation compared to the NOTIDE simulation.

These two examples from the El Niño and La Niña periods illustrate how the regular tidal barotropic forcing introduces vary different internal tide signals within the Solomon Seas, with greatly contrasting

https://doi.org/10.5194/os-2019-94
Preprint. Discussion started: 26 September 2019

effects on the regional circulation and EKE field, and on surface water characteristics : reducing the surface cooling during El Niño, increasing the surface warming during the La Niña period. The surface modifications induced by the interaction of the internal tides with the mesoscale circulation have a strong implication for the regional ocean/atmosphere interactions.

6. Discussion/Conclusion

We have analyzed here the role of internal tides in the Solomon Sea and their impact on the circulation and the surface and subsurface water masses, based on two regional simulations with and without tides. Since the interaction of the internal tide with the background circulation has strong nonlinear interactions, and the energy cascade between them can cover similar space-time scales, its not easy to cleanly separate the two signals from a single model. In our model set-up, having 2 distinct models with and without tides but with the same resolution and surface forcing has allowed us to fully explore the impacts of introducing the barotropic and baroclinic tides into a regional circulation model, for both the phase-locked and non phase-locked components.

Since the Solomon Sea is under the influence of ENSO, the characteristics of the internal tides were analyzed for two contrasted ENSO conditions: the 1997-1998 El Niño and the 1999 La Niña. These are two extreme events with strong stratification changes in the western Pacific and Solomon Seas, and provide good case studies for investigating the impact of the internal tides on the regional circulation and water mass transformation. We are conscious though that we have only analyzed one El Niño and one La Niña event, each over a limited 3-month period of hourly averages, which is insufficient to conclude on the influence of ENSO on the internal tides. Indeed, 3-months is roughly twice the mesoscale eddy decorrelation time in the tropics but it is also the local residence time for surface waters flowing through the Solomon Sea (Melet et al, 2011). A longer simulation, including more contrasted El Niño/La Niña events, would be needed to better characterize the response of the tides to the ENSO variability. Nevertheless, these two contrasted events are sufficiently different to qualitatively describe the changes induced in the internal tide field.

Within the Solomon Seas, the M2 barotropic tide is rather weak but its interaction with the strong topographic features (islands, shelves, deep ocean ridges) generates the strongest component of the internal tide. Although the M2 Mode 1 is the dominant mode to propagate baroclinic tidal energy within the Solomon Sea, during the El Niño period, with the peak in N^2 stratification being closer to the surface, more energy becomes partitioned into mode 2. This is important since studies that aim to predict and remove the internal tide from altimetric SSH observations, before calculating geostrophic currents, may use an empirical "all mode" fitting of the M2 internal tide (eg Ray and Zaron, 2016) or concentrate only on mode1 (Zhao et al., 2016). In this Solomon Sea region, with strong stratification changes, we need at least modes 1 and 2.

We have concentrated on this M2 component for our study, to simplify the presentation, but other modes are also energetic (S2, M4, K1, O1; Figure 6). The second highest baroclinic tide mode is S2, which is well observed by the current Topex/Jason altimeter orbits and also in the future SWOT mission, whose orbit is designed to characterize the 2D structure of the tides and internal tides (Fu et al., 2009; Morrow et al., 2019). Other altimeters on a sun-synchronous orbit (Envisat, Saral-AltiKa, Sentinel-3, planned future wide-swath missions) will not be able to observe this S2 12h cycle, which

https://doi.org/10.5194/os-2019-94
Preprint. Discussion started: 26 September 2019

poses a problem for the understanding of the S2 internal tide, its interaction with the changing ocean circulation, and the validation of models with tides in the future (post SWOT). Future studies are needed to investigate the impacts of the S2 internal tide in the Solomon Sea and in the tropics.

We find that the generation, propagation and dissipation of the internal tides are sensitive to changes in stratification and to the mesoscale activity that occurs between these two El Niño and La Niña cases. The La Niña period with its high level of mesoscale activity and deeper stratification favors the appearance of more non phase-locked internal tides. So the strong mesoscales are refracting, scattering and eventually dissipating the internal tide field that propagated away from its generation sites, contributing to the increase in the non phase-locked component. However, the modified EKE fields, particularly during La Niña, highlight how the mesoscale turbulence is also being constantly perturbed and destabilized by the internal tides hitting their sides every 12-24 hours! The role of internal tides providing an additional instability mechanism for the oceanic energy cascade remains an unknown theoretical problem, and continuing work is needed to understand these interactions with realistic models and observations.

Where and how the 1 TW of global internal tide energy is dissipated in the open ocean has also been a long-standing question (Egbert and Ray, 2000). The dissipation of internal tides may occur right after generation or after radiation away from the generation sites. Our analysis showed that most dissipation occurs locally (from 60 to 80%), but that the proportion of local to far-field dissipation varies during the El Niño or La Niña periods. For example, during la Niña, there is a lower baroclinic tide generation in the Solomon Strait box, thus less local dissipation, but an increase in the far field dissipation between 7 and 8°S that is quite significant. This may be influenced by the interaction of the EKE with the southward propagative internal tides generated in the Solomon Strait, but highlights the variability in the dynamical interactions, and the complications this introduces in the energy budget estimations (see Table 1).

Models do not resolve the sum of the processes responsible for dissipation, but if sufficiently validated, may provide some clues of possible internal tide dissipation at regional scales. Estimate for the dissipation in OGCMs is done following equation (1). This equation does not take into account the non-linear advection (Buijsman et al. 2016) that might be contained in the dissipation estimate. This might overemphasize the energy of our dissipation estimates. But no data has been used to quantify the actual bias in these energy terms. This is work for future research.

The divergence of the baroclinic flux and the conversion rate integrated over the Solomon Sea shows that all of the baroclinic tidal energy is dissipated within the Solomon Sea. This confirms the hypothesis inherent in the tidal diffusivity parameterization included in the regional simulation of the Solomon Sea by Melet et al. (2011). Although this parameterization does not allow a detailed analysis of the internal-tide-circulation interactions as presented here, it potentially allows us to include the effects of the internal tide mixing and dissipation for marginal seas in a low resolution global ocean or climate model. At this stage it is not obvious to compare precisely our results with those from the tidal parameterization of Melet et. al. (2011) since important progress has been made in the modelling. For example, the bias of 0.1 psu observed in Melet et al. (2011) in the Solomon Sea has now been reduced to 0.02 psu. Also the Melet et al. (2011) results are based on climatology and a monthly annual cycle whereas our results are based on a three year simulation with high-frequency atmospheric and tidal forcing. Yet both our TIDES model and the model with tidal parameterizations show a weakening of salinities in and downstream of the Solomon Sea. The zonal salinity gradient observed in CARS across the Solomon Islands exists in both simulations, but is stronger when using the tidal parameterization than in CARS or in the simulation with tides. Upstream of the Solomon Sea, the salt minima observed in CARS in the Bismarck Sea and along the northern coast of Papua New Guinea (Fig. 1) are also better reproduced when introducing the tidal effect but the effect of the tidal parameterization is stronger (a 0.2 psu correction) by a factor of 10 than in the simulation with tides (0.02 psu correction). So including the tidal parameterization in our NOTIDES model that is relatively accurate may degrade the simulation with nonrealistic fresh salinities. It argues for the use of a model with explicit tides. We have not specifically compared the circulation changes between our model with TIDES, and the NOTIDES version including the internal tide parameterization, but again it would be an interesting subject for a future study.

Our modeling results show that the diapycnal mixing induced by the internal tides is particularly useful to erode the salinity maximum of the upper thermocline water, and to cool the surface temperature interacting with the atmosphere. Such effects are particularly visible far from the strong currents, where particles may experience the effect of tide during a longer time. Nevertheless, the impacts may be radically different when considering particular ENSO conditions over the shorter 3-month period. For example, the interaction of the internal tides with the surface mesoscale activity during La Niña, tends to further warm the SST field with possible impacts on regional air sea interactions. Although a coupled ocean-atmosphere climate model that includes the effects of the explicit tidal forcing is not on the horizon, it would be interesting in the future to include the tidal parameterization for this marginal sea in a coupled model, given its key position upstream of the equatorial Pacific circulation.

Acknowledgements
This work is part of M. Tchilibou's PhD thesis funded by the University of Toulouse III. L. Gourdeau and A. Koch-Larrouy are funded by IRD; R. Morrow is funded by CNAP, F. Lyard and D. Allain by CNRS and B. Djath was funded by CNES. The paper benefited from discussions with J. Jouanno from LEGOS. This work is a contribution to the joint CNES/NASA SWOT project "SWOT in the tropics" and is supported by the French TOSCA programme.

References

Alberty, M. S., Sprintall J., MacKinnon J., Ganachaud A., Cravatte S., Eldin G., Germineaud C., and Melet A.: Spatial patterns of mixing in the Solomon Sea, J. Geophys. Res. Oceans,122, https://doi.org/10.1002/2016JC012666, 2017.

Arbic, B., Wallcraft, J., Metzger, J.: Concurrent simulation of the eddying general circulation and tides in a global ocean model, Ocean Mod., 32(3-4), 175 – 187, 2010.

Buijsman, M. C., Arbic B. K., Richman J. G., Shriver J. F., Wallcraft A. J., and Zamudio, L.: Semidiurnal internal tide incoherence in the equatorial Pacific, J. Geophys. Res. Oceans, 122, https://doi.org/10.1002/2016JC012590, 2017.

Cabanes, C., Grouazel, A., Von Schuckmann, K., Hamon, M., Turpin, V., Coatanoan, C., Paris, F., Guinehut, S., Boone, C., Ferry, N., De Boyer Montegut, C., Carval, T., Reverdin, G., Pouliquen, S., Le Traon, P.Y.: The CORA dataset: validation and diagnostics of in-situ ocean temperature and salinity measurements. Ocean Science, 9(1), 1-18, https://doi.org/10.5194/os-9-1-2013, 2013.

https://doi.org/10.5194/os-2019-94
Preprint. Discussion started: 26 September 2019

Ocean Science
Discussions

Carrere, L., Lyard, F., Cancet, M., Guillot, A.: FES 2014, a new tidal model on the global ocean with enhanced accuracy in shallow seas and in the Arctic region. Geophysical Research Abstracts, vol. 17. EGU2015-5481-1, EGU General Assembly, 2015.

Carter, G.S., Merrifield M.A., Becker J.M., Katsumata K., Gregg M.C., Luther D.S., Levine M.D., Boyd T.J., and Firing Y.L.: Energetics of M2 Barotropic-to-Baroclinic Tidal Conversion at the Hawaiian Islands. J. Phys. Oceanogr., 38, 2205-2223, https://doi.org/10.1175/2008JPO3860.1, 2008

Chavanne, C. , Flament, P., Carter, G., Merrifield, M., Luther, D., Zaron, E., and Gurgel, K. W.: The Surface Expression of Semidiurnal Internal Tides near a Strong Source at Hawaii. Part I: Observations and Numerical Predictions. J. Phys. Oceanogr., 40(6), 1155-1179, 2010

Cravatte, S., Ganachaud, A., Duong, Q.-P., Kessler, W. S., Eldin, G., and Dutrieux, P.: Observed circulation in the Solomon sea from SADCP data, Prog. Oceanogr., 88(1-4), 116–130, https://doi.org/10.1016/j.pocean.2010.12.015, 2011

Davis, R. E., Kessler, W. S., and Sherman, J. T.: Gliders measure western boundary current transport from the south pacific to the equator, J. Phys. Oceanogr., 42(11), 2001–2013, https://doi.org/10.1175/JPO-D-12-022.1., 2012.

Dee, D. P., Uppala, S. M., Simmons, A. J., Berrisford, P., Poli, P., Kobayashi, S., Andrae, U., Balmaseda, M. A., Balsamo, G., Bauer, P., Bechtold, P., Beljaars, A. C. M., van de Berg, L., Bidlot, J., Bormann, N., Delsol, C., Dragani, R., Fuentes, M., Geer, A. J., Haimberger, L., Healy, S. B., Hersbach, H., Helm, E. V., Isaksen, L., Kallberg, P., Kahler, M., Matricardi, M., McNally, A. P., Monge-Sanz, B. M., Morcrette, J.-J., Park, B.-K., Peubey, C., de Rosnay, P., Tavolato, C., Thepaut, J.-N., and Vitart, F.: The ERA-Interim reanalysis: configuration and performance of the data assimilation system, Q. J. Roy. Meteorol. Soc., 137, 553–597, https://doi.org/10.1002/qj.828, 2011.

Djath, B., Verron, J., Melet, A., Gourdeau, L., Barnier, B., and Molines, J.-M.: Multiscale dynamical analysis of a high-resolution numerical model simulation of the Solomon Sea circulation, J. Geophys. Res.-Oceans, 119, 6286–6304, https://doi.org/10.1002/2013JC009695, 2014.

Dushaw, B. D.: An empirical model for mode-1 internal tides derived from satellite altimetry: Computing accurate tidal predictions at arbitrary points over the world oceans (Tech. Rep.) Washington: Applied Physics Laboratory, University of Washington, 2015

Egbert, G., and Ray, R.: Significant dissipation of tidal energy in the deep ocean inferred from satellite altimeter data, Nature, 405, 775 – 778, 2000.

Egbert, G. D., and Ray, R. D.: Tidal prediction, Journal of Marine Research, *75*, 1–49, 2017.

Fine, R. A., Lukas R., Bingham F., Warnar M., and Gammon R.: The western equatorial Pacific: A water mass crossroads, J. Geophys. Res., 99, 25 063–25 080, 1994.

Fu, L-L., E Rodriguez, D Alsdorf, R. Morrow (eds). (2012). SWOT Mission Science document. JPL Publication. https://swot.jpl.nasa.gov/files/swot/SWOT_MSD_1202012.pdf

Ganachaud, A., Cravatte, S., Melet, A., Schiller, A., Holbrook, N. J., Sloyan, B. M.,Widlansky, M. J., Bowen, M., Verron, J.,Wiles, P., Ridgway, K., Sutton, P., Sprintall, J., Steinberg, C., Brassington, G., Cai, W., Davis, R., Gasparin, F., Gourdeau, L., Hasegawa, T., Kessler, W., Maes, C., Takahashi, K., Richards, K. J., and Send, U.: The Southwest Pacific Ocean circulation and climate experiment (SPICE), J. Geophys. Res.-Oceans, 119, 7660–7686, https://doi.org/10.1002/2013JC009678, 2014.

Gasparin, F., Ganachaud A., Maes C., Marin F., and Eldin G.: Oceanic transports through the Solomon sea: The bend of the New Guinea coastal undercurrent, Geophys. Res. Lett., 39, L15608, https://doi.org/10.1029/2012GL052575, 2012.

https://doi.org/10.5194/os-2019-94
Preprint. Discussion started: 26 September 2019

Germineaud, C., Ganachaud, A., Sprintall, J., Cravatte, S., Eldin, G., Alberty, M. S., and Privat, E.: Pathways and water mass properties of the thermocline and intermediate waters in the Solomon Sea. J. Phys. Oceanogr., 46 (10), 3031-3049. ISSN 0022-3670

Gourdeau, L.: Internal tides observed at 2°S-156°E by in situ and TOPEX/POSEIDON data during COARE, J. Geophys. Res.-Oceans, 103, 12629-12638, 1998.

Gourdeau, L., Verron, J., Melet, A., Kessler, W., Marin, F., and Djath, B.: Exploring the mesoscale activity in the Solomon Sea: a complementary approach with numerical model and altimetric data, J. Geophys. Res.-Oceans, 119, 2290–2311, https://doi.org/10.1002/2013JC009614, 2014.

Gourdeau, L., Verron, J., Chaigneau, A., Cravatte, S., and Kessler, W.: Complementary use of glider data, altimetry, and model for exploring mesoscale eddies in the tropical Pacific Solomon Sea, J. Geophys. Res.-Oceans, 122, 9209–9229, https://doi.org/10.1002/2017JC013116, 2017.

Grenier, M., Cravatte, S., Blanke, B., Menkes, C., Koch-Larrouy, A., Durand, F., Melet, A., and Jeandel, C.: From the western boundary currents to the pacific equatorial undercurrent: Modeled pathways and water mass evolutions, J. Geophys. Res.-Oceans, 116, C12044, https://doi.org/10.1029/2011JC007477, 2011.

Hristova, H. G., and Kessler, W. S.: Surface circulation in the Solomon Sea derived from Lagrangian drifter observations, J. Phys. Oceanogr., 42(3), 448–458, https://doi.org/10.1175/JPO-D-11-099.1, 2012.

Hristova, H. G., Kessler, W. S., McWilliams, J. C., and Molemaker, M. J.: Mesoscale variability and its seasonal variability in the Solomon and coral seas, J. Geophys. Res.-Oceans, 119, 4669–4687, https://doi.org/10.1002/2013JC009741, 2014.

Kelly, S. M., Nash, J. D., and Kunze, E.: Internal-tide energy over topography, J. Geophys. Res.-Oceans, 115, C06014, https://doi.org/10.1029/2009JC005618, 2010.

Kelly, S.M., Nash, J.D., Martini, K.I., Alford, M.H., and Kunze, E.: The Cascade of Tidal Energy from Low to High Modes on a Continental Slope, J. Phys. Oceanogr., 42, 1217-1232, https://doi.org/10.1175/JPO-D-11-0231.1, 2012.

Kessler, W.S., Hristova, H.G., Davis, R.E., and Sherman, J.T.: Equatorward western boundary transport from the South Pacific: Glider observations, dynamics and consequences. Prog. Oceanogr., 175, 208-225, https://doi.org/10.1016/j.pocean.2019.04.005, 2019.

Koch-Larrouy, A., Madec, G., Bouruet-Aubertot, P., Gerkema, T., Bessières, L., Molcard, R.: On the transformation of Pacific Water into Indonesian Throughflow Water by internal tidal mixing, Geophys. Res. Lett., 34, (L04604), 2007.

Koch-Larrouy, A., Lengaigne, M., Masson, S., Madec, G., Terray, P.: Indonesian tidal mixing effect on climate system, Clim. Dyn., http://dx.doi.org/10.1007/s00382-009-0642-4, 2010.

Koch-Larrouy, A., Atmadipoera, A., van Beek, P., Madec, G., Aucan, J., Lyard, F., Grelet, J., Souhaut, M.: Estimates of tidal mixing in the Indonesian archipelago from multidisciplinary INDOMIX *in-situ* data, Deep-Sea Res. I, 106, 136 - 153, 2015.

Large, W., and Yeager, S.: The global climatology of an interannually varying air-sea flux data set, Clim. Dyn., 33, 341–364, 2009.

Levitus, S., Boyer, T. P., Conkright, M. E., O'Brien, T., Antonov, J., Stephens, C., and Gelfeld, R.: NOAA Atlas NESDIS 18,World Ocean Data base 1998: VOLUME 1: Introduction, US Gov. Printing Office, Washington, D.C., 346 pp., 1998.

Madec, G.: NEMO ocean engine, Note du Pole de Modélisation, Tech. Rep. 27, Inst. Pierre Simon Laplace, France, 300 pp., 2008.

https://doi.org/10.5194/os-2019-94
Preprint. Discussion started: 26 September 2019

Melet, A., Gourdeau, L., Kessler, W. S., Verron, J., and Molines, J.-M.: Thermocline circulation in the Solomon Sea: A modeling study, J. Phys. Oceanogr., 40(6), 1302–1319, https://doi.org/10.1175/2009JPO4264.1, 2010a.

Melet, A., Gourdeau, L., and Verron, J.: Variability in Solomon sea circulation derived from altimeter sea level data, Ocean Dyn., 60(4), 883–900, doi:10.1007/s10236-010-0302-6, 2010b.

Melet, A., Verron, J., Gourdeau, L., and Koch-Larrouy, A.: Equatorward pathways of Solomon sea water masses and their modifications, J. Phys. Oceanogr., 41, 810–826, https://doi.org/10.1175/2010JPO4559.1, 2011.

Melet, A., Gourdeau, L., Verron, J., and Djath, B.: Solomon sea circulation and water mass modifications: Response at ENSO timescales, Ocean Dyn., 63(1), 1–19, https://doi.org/10.1007/s10236-012-0582-0, 2013.

Morrow, R., Fu, L. L., Ardhuin, F., Benkiran, M., Chapron, B., Cosme, E., D'Ovidio, F., Farrar, J. T., Gille, S. T.,Lapeyre, G., Le Traon, P. Y., Pascual, A., Ponte, A., Qiu, B., Rascle, N., Ubelmann, C., Wang, J;, Zaron, E. D.: Global observations of fine-scale ocean surface topography with the Surface Water and Ocean Topography (SWOT) Mission, OceanObs2019, Frontiers in Marine Science, https://doi/org/ 10.3389/fmars.2019.00232, 2019.

Munk, W.H., and Wunsch, C.: Abyssal recipes II: energetics of tidal and wind mixing, Deep Sea Res. I, 45, 1977–2010. http://dx.doi.org/10.1016/S0967-0637(98)00070-3, 1998.

Müller, M., Cherniawsky, J. Y., Foreman, M. G. G., and von Storch, J.-S.: Global M2 internal tide and its seasonal variability from high resolution ocean circulation and tide modeling, Geophys. Res. Lett., 39, L19607, https://doi.org/10.1029/2012GL053320, 2012.

Nagai, T., and Hibiya, T.: Internal tides and associated vertical mixing in the Indonesian Archipelago, J. Geophys. Res.-Oceans, 120, 3373–3390, doi:10.1002/2014JC010592, 2015.

Nash J.D., Kunze, E., Lee, C. M., and Sanford, T. B.: Structure of the baroclinic tide generated at Kaena Ridge, Hawaii. J. Phys. Oceanogr., 36, 1123–1135, 2006.

Nash, J.D., Kelly, S.M., Shroyer, E.L., Moum, J. N., and Duda, T. F.: The unpredictable nature of internal tides and nonlinear waves on continental shelves, J. Phys. Oceanogr., 42, https://doi.org/ 10.1175/JPO-D-12-028.1, 2012.

Niwa, Y., and Hibiya, T.: Numerical study of the spatial distribution of the M2 internal tide in the Pacific Ocean, J. Geophys. Res., 106, 22,441– 22,449, 2001.

Niwa, Y., and Hibiya, T.: Three-dimensional numerical simulation of M2 internal tides in the East China Sea, J. Geophys. Res., 109, C04027, https://doi.org/10.1029/2003JC001923, 2004.

Niwa, Y., and Hibiya, T.: Estimation of baroclinic tide energy available for deep ocean mixing based on three-dimensional global numerical simulations, J. Oceanogr. 67, 493–502. https://doi.org/10.1007/s10872-011-0052-1, 2011.

Niwa, Y., and Hibiya, T.: Generation of baroclinic tide energy in a global three-dimensional numerical model with different spatial grid resolutions, Ocean Modelling, 80, 59-73, https://doi.org/10.1016/j.ocemod.2014.05.003, 2014.

Nugroho, D., Koch-Larrouy, A., Gaspar, P., Lyard, F., Reffray, G., and Tranchant, B.: Modelling explicit tides in the Indonesian seas: An important process for surface sea water properties, Mar. Poll. Bull. 131(b), 7 – 18, 2017.

Qin, X., Menviel, L., Sen Gupta, A., and van Sebille, E.: Iron sources and pathways into the Pacific Equatorial Undercurrent, Geophys. Res. Lett., 43, https://doi.org/10.1002/2016GL070501, 2016.

Price, J.F., and Yang, J.: Marginal Sea Overflows for Climate Simulations and Parameterizations, E.P. Chassignet and J. Verron (Eds.), Kluwer Academic Publishers, 155-170, 1998.

https://doi.org/10.5194/os-2019-94
Preprint. Discussion started: 26 September 2019

Ocean Science
Discussions
Open Access

Ray, R. D., and Zaron, E.: M2 internal tides and their observed wavenumber spectra from satellite altimetry, J. Phys. Oceanogr., 46(1), 3–22, https://doi.org/10.1175/JPO-D-15-0065.1, 2016.

Qiu, B., and Chen, S.: Seasonal modulations in the Eddy field of the South Pacific Ocean, J. Phys. Oceanogr., 34, 1515–1527, 2004.

Qu, T., and Lindstrom, E. J.: Northward intrusion of Antarctic intermediate water in the western Pacific, J. Phys. Oceanogr., 34(9), 2104–2118, https://doi.org/10.1175/1520-0485(2004)034<2104:NIOAIW>2.0.CO;2, 2004.

Rudnick, D. L., Johnston, T. M. S., and Sherman, J. T.: High-frequency internal waves near the Luzon Strait observed by underwater gliders, J. Geophys. Res.-Oceans, 118, 774–784, https://doi.org/10.1002/jgrc.20083, 2013.

Savage, A. C., Arbic, B. K., Richman, J. G., Shriver, J. F., Alford, M. H., Buijsman, M. C., Farrar, J. T., Sharma, H., Voet, G., Walcraft, A. J., and Zmudio., L. : Frequency content of sea surface height variability from internal gravity waves to mesoscale eddies, J. Geophys. Res.-Oceans, 122, 2519–2538, https://doi.org/10.1002/2016JC012331, 2017.

Shriver, J., Arbic, B., Richman, J., Ray, R., Metzger, E., Wallcraft, A., and Timko, P.: An evaluation of the barotropic and internal tides in a high-resolution global ocean circulation mode. J. Geophys. Res.-Oceans 117(C10), 2012.

Shriver, J., Richman, J., and Arbic, B.: How stationary are the internal tides in a high-resolution global ocean circulation model?, J. Geophys. Res.-Oceans, 119, 2769 - 2787, 2014.

Simmons, H., Jayne, S., St. Laurent, L., and Weaver, J.: Tidally driven mixing in a numerical model of the ocean general circulation, Ocean Mod., 6(3-4), 245 – 263, 2004.

Srinivasan, K., McWilliams, J.C., Renault, L., Hristova, H.G., Molemaker, J., and Kessler, W.S.: Topographic and Mixed Layer Submesoscale Currents in the Near-Surface Southwestern Tropical Pacific, J. Phys. Oceanogr., 47, 1221-1242, https://doi.org/10.1175/JPO-D-16-0216.1, 2017.

Tchilibou, M., Gourdeau, L., Morrow, R., Serazin, G., Djath, B., and Lyard, F.: Spectral signatures of the tropical Pacific dynamics from model and altimetry: a focus on the meso-/submesoscale range, Ocean Sci., 14, 1283-1301, https://doi.org/10.5194/os-14-1283-2018, 2018.

Treguier, A. M., Barnier, B., deMiranda, A. P., Molines, J. M., Grima, N., Imbard, M., Madec, G., Messager, C., Reynaud, T., and Michel, S.: An eddy-permitting model of the Atlantic circulation: Evaluating open boundary conditions, J. Geophys. Res., 106, 22115–22129, https://doi.org/10.1029/2000JC000376, 2001.Tsuchiya, M., R. Lukas, R. Fine, E. Firing, and E. Lindstrom, 1989: Source waters of the Pacific Equatorial Undercurrent. Prog. Oceanogr., 23, 101–147.Wunsch 1975

Zaron, E. D., and Egbert, G. D.: Time-variable refraction of the internal tide at the Hawaiian Ridge, J. Phys. Oceanogr., 44(2), 538–557, 2014.

Zaron, E. D.: Mapping the nonstationary internal tide with satellite altimetry, J. Geophys. Res.-Oceans, 122, 539–554, https://doi.org/10.1002/2016JC012487, 2017.

Zhao, Z., Alford, M. H., MacKinnon, J. A., and Pinkel, R.: Long-range propagation of the semidiurnal internal tide from the Hawaiian Ridge. J. Phys. Oceanogr., 40, 713–736, https://doi.org/10.1175/2009JPO4207.1, 2010.

Zhao, Z., Alford, M. H., Girton, J. B., Rainville, L., and Simmons, H. L.: Global observations of open-ocean mode-1 M2 internal tides. J. Phys. Oceanogr., 46, 1657–1684. https://doi.org/10.1175/JPO-D-15-0105.1, 2016.

Zhao, Z.: The global mode-2 M2 internal tide. J. Geophys. Res.-Oceans, 123, 7725–7746. https://doi.org/10.1029/2018JC014475, 2018.

https://doi.org/10.5194/os-2019-94
Preprint. Discussion started: 26 September 2019

	Div(FBT)		DBT		CVR		Div(FBC)		DBC		P1 %		P2 %	
	Niño	Niña	Niño	Niña	Niño	Niña	Niño	Niña	Niño	Niña	Niño	Niña	Niño	Niña
Sol str	3.	2.93	- 0.84	- 0.86	-2.16	- 2.07	0.53	0.7	- 1.63	- 1.37	72	71	75	66
Sol sud	6.83	5.89	- 2.53	- 2.11	-4.3	- 3.78	1.27	0.75	- 3.03	- 3.03	63	64	70	80
PNG	1.75	1.81	- 0.38	- 0.45	-1.37	- 1.36	0.76	0.73	- 0.64	- 0.63	79	75	47	46

Table 1: Div(FBT) (Div(FBC)) is the divergence of the barotropic (baroclinic) flux, DBT (DBC) is the dissipation of the barotropic (baroclinic) flux, CVR is the conversion rate from barotropic to baroclinic energy. Units are in GW. P1 is the percentage of the barotropic energy converted into baroclinic energy and P2 is the percentage of the baroclinic energy dissipated within the box.

Figure captions

Figure 1: Bathymetry of the Solomon Sea (in color, unit in m). The 50 m depth has a black contour. PNG: Papua New Guinea, NB: New Britain, NI: New Ireland, Vit. Str.: Vitiaz strait, Sol. Str.: Solomon Strait, Wdl arch.: Woodlark Archipelago. The arrows illustrate the different currents mentioned in the text (Dashed arrows are for surface currents, line arrows are for the thermocline currents). NGCC: New Guinea Coastal Current, NGCU: New Guinea Coastal UnderCurrent, SSI: Solomon Strait Inflow, EUC: Equatorial UnderCurrent, SEC: South Equatorial Current, NVJ: North Vanuatu Jet, GPC: Gulf of Papua Current. The bathymetric file is the NOAA/ETOPO2v2 bathymetric file from the Smith & Sandwell database (doi: 10.7289/V5J1012Q).

Figure 2: Mean surface EKE (shading, unit : cm^2/s^2) and mean surface circulation (arrows) from the 3-month TIDE simulations during a) the El Niño state and b) the La Niña state. White color is for bathymetry less than 50 m depth. Isobathymetric lines are from the NOAA/ETOPO2v2 bathymetric file from the Smith & Sandwell database (doi: 10.7289/V5J1012Q).

Figure 3: Root-mean-square of SSH variability for the 3-month periods of the El Niño state (left column) and of the La Niña state (right column). Unit is in cm. The top panel is the full SSH variance, the second panel is the mesoscale variability (periods > 48h), the third panel is the high frequency variability (periods < 48h), dominated by the internal tides (both coherent and incoherent components) and the bottom panel is the incoherent internal tide variability. Note the change of colorbar for the full and mesoscale variability of the La Niña period. Isobathymetric lines are from the NOAA/ETOPO2v2 bathymetric file from the Smith & Sandwell database (doi: 10.7289/V5J1012Q).

Figure 4: Latitude/depth section at 154°E of mean salinity from a) the R36Td simulation, b) CARS climatology, and of salinity anomalies for the 3 month c) El Niño period and d) La Niña period, relative

https://doi.org/10.5194/os-2019-94
Preprint. Discussion started: 26 September 2019

Ocean Science
Discussions
Open Access

to the full R36Td period. The Solomon Sea section is between the topographic features (vertical black lines) at 12°S and 6°S.

Figure 5: Mean N^2 profile averaged for the Solomon Sea section at 154°E from CARS climatology (Cyan), and from the R36Td TIDES simulation averaged over the entire 3-year period (blue), the 3-month El Niño period (green) and the 3-month La Niña period (red). The dash blue line is for the R36d NOTIDES simulation averaged over the entire 3-year period. Unit is in s^{-1}.

Figure 6: a) SSH frequency spectra averaged over the Solomon Sea area based on the 3 month hourly outputs of the El Niño period for the R36h simulation (No tides, in cyan), for the R36Th simulation including barotropic and baroclinic tides (Tides, in blue), baroclinic tides only (Tides-BT, in green), incoherent baroclinic tides only (Tides-BT-BC, in red). b) Zoom on SSH frequency spectra showing the diurnal, semidiurnal, and quart diurnal signature of baroclinic tides calculated during the El Niño period (in red) and the La Niña period (in green). For clarity the green spectrum is shifted by 2 hours.

Figure 7: SSH M2 barotropic tide from a) FES2014, and b) the R36Th simulation. Amplitude is in color (unit in cm) and the contours are phase lines. Isobathymetric lines are from the NOAA/ETOPO2v2 bathymetric file from the Smith & Sandwell database (doi: 10.7289/V5J1012Q).

Figure 8: SSH amplitude of the stationary M2 baroclinic tide as estimated from a) altimetry by Ray and Zaron (2016), the R36Th simulations during the 3-months of b) the El Niño period, and c) the La Niña period. Unit in cm. Isobathymetric lines are from the NOAA/ETOPO2v2 bathymetric file from the Smith & Sandwell database (doi: 10.7289/V5J1012Q).

Figure 9: Conversion rate (top), the baroclinic flux divergence (middle), and the dissipation rate (bottom) for the M2 harmonic (negative values shaded in blue, positive values in red, unit: Wm^{-2}). The corresponding barotropic and baroclinic energy flux are superimposed with arrows in the top and middle panels, with a scaling of 50 kWm^{-1} and 2 kWm^{-1}, respectively. The left column corresponds to the El Niño period and the right column to the La Niña period. The boxes define the different generation areas where energetics are quantified in Table 1. Isobathymetric lines are from the NOAA/ETOPO2v2 bathymetric file from the Smith & Sandwell database (doi: 10.7289/V5J1012Q).

Figure 10: Modal decomposition of the M2 energy flux during the 3-month El Niño (top) and La Niña (bottom) periods, corresponding to mode 1 (left), and mode 2 (right). The shading is the amplitude (unit in Wm^{-1}). Isobathymetric lines are from the NOAA/ETOPO2v2 bathymetric file from the Smith & Sandwell database (doi: 10.7289/V5J1012Q).

Figure 11: Vertical section at 154°E of the mean meridional energy flux estimated during a) El Niño state and b) La Niña state (unit in Wm^{-1}). The corresponding isopycnals are in contours; with □ = 23.5 and □=24.5 in bold.

Figure 12: Mean difference in temperature (left, unit in °C) and salinity (right) between the simulation with tides and the simulation without tides (TIDES-NOTIDES) for the surface waters (SW, top), the upper thermocline waters (UTW, middle), and the intermediate waters (IW, bottom). The density range for these water masses are defined in the text. Isobathymetric lines are from the NOAA/ETOPO2v2 bathymetric file from the Smith & Sandwell database (doi: 10.7289/V5J1012Q).

https://doi.org/10.5194/os-2019-94
Preprint. Discussion started: 26 September 2019

Ocean Science
Discussions
Open Access

Figure 13: Mean salinity distribution in the UTW waters from the 3-year a) NOTIDE simulation, b) TIDE simulation, and c) the multi-decadal CARS climatology. Isobathymetric lines are from the NOAA/ETOPO2v2 bathymetric file from the Smith & Sandwell database (doi: 10.7289/V5J1012Q).

Figure 14: Temperature anomalies at 30 m depth relative to the 3 year mean average (shading, °C) over the El Niño period (left) and the La Niña period (right) for the NOTIDE simulation (a and b) and the TIDE simulation (c and d). Superimposed contours are the corresponding EKE field. EKE contours are plotted for values higher than 400 cm^2/s^2, every 400 cm^2/s^2. Bottom panels : difference in SST (shading, °C) and in EKE (contour, cm^2/s^2) between the TIDE and NOTIDE simulations averaged over e) the El Niño period, and f) the La Niña period. The black line and black dash contours are for positive and negative EKE differences, respectively; and contours are plotted every 400 cm^2/s^2. Isobathymetric lines are from the NOAA/ETOPO2v2 bathymetric file from the Smith & Sandwell database (doi: 10.7289/V5J1012Q).

https://doi.org/10.5194/os-2019-94
Preprint. Discussion started: 26 September 2019

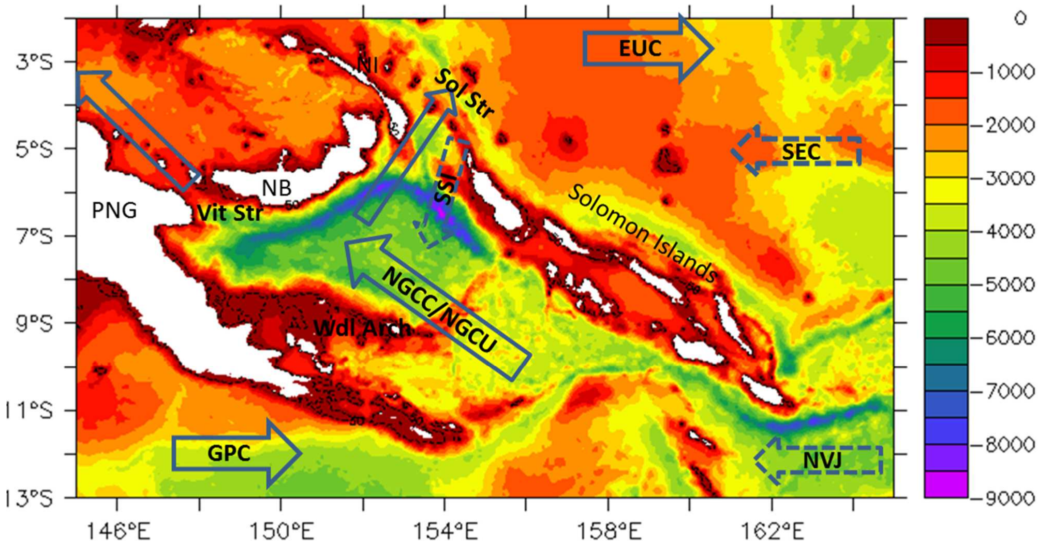

Figure 1: Bathymetry of the Solomon Sea (in color, unit in m). The 50 m depth has a black contour. PNG: Papua New Guinea, NB: New Britain, NI: New Ireland, Vit. Str.: Vitiaz strait, Sol. Str.: Solomon Strait, Wdl arch.: Woodlark Archipelago. The arrows illustrate the different currents mentioned in the text (Dashed arrows are for surface currents, line arrows are for the thermocline currents). NGCC: New Guinea Coastal Current, NGCU: New Guinea Coastal UnderCurrent, SSI: Solomon Strait Inflow, EUC: Equatorial UnderCurrent, SEC: South Equatorial Current, NVJ: North Vanuatu Jet, GPC: Gulf of Papua Current. The bathymetric file is the NOAA/ETOPO2v2 bathymetric file from the Smith & Sandwell database (doi: 10.7289/V5J1012Q).

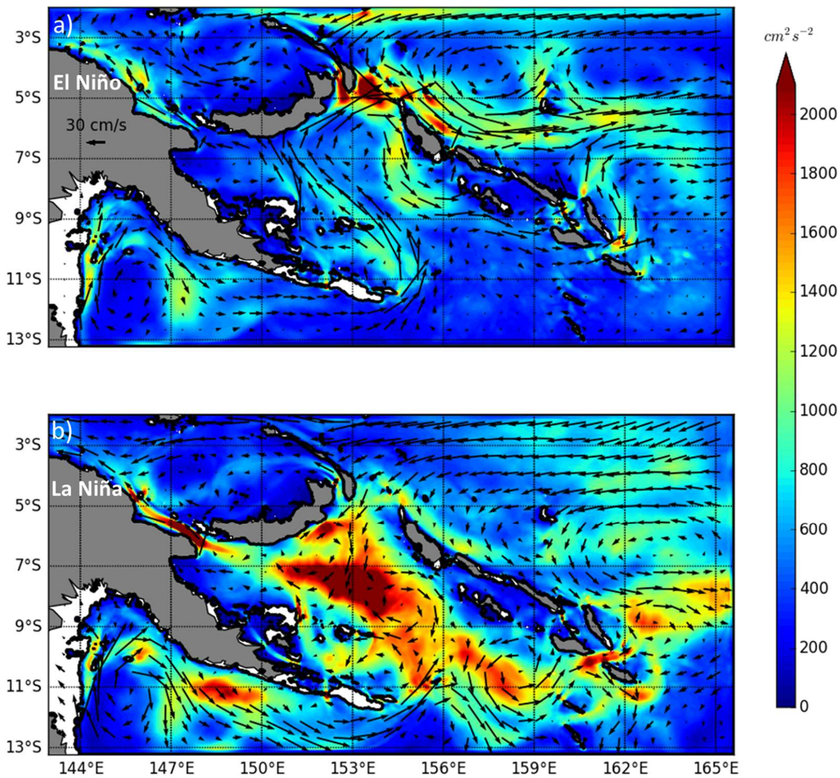

Figure 2: Mean surface EKE (shading, unit : cm^2/s^2) and mean surface circulation (arrows) from the 3-month TIDE simulations during a) the El Niño state and b) the La Niña state. White color is for bathymetry less than 50 m depth. Isobathymetric lines are from the NOAA/ETOPO2v2 bathymetric file from the Smith & Sandwell database (doi: 10.7289/V5J1012Q).

https://doi.org/10.5194/os-2019-94
Preprint. Discussion started: 26 September 2019

Ocean Science
Discussions

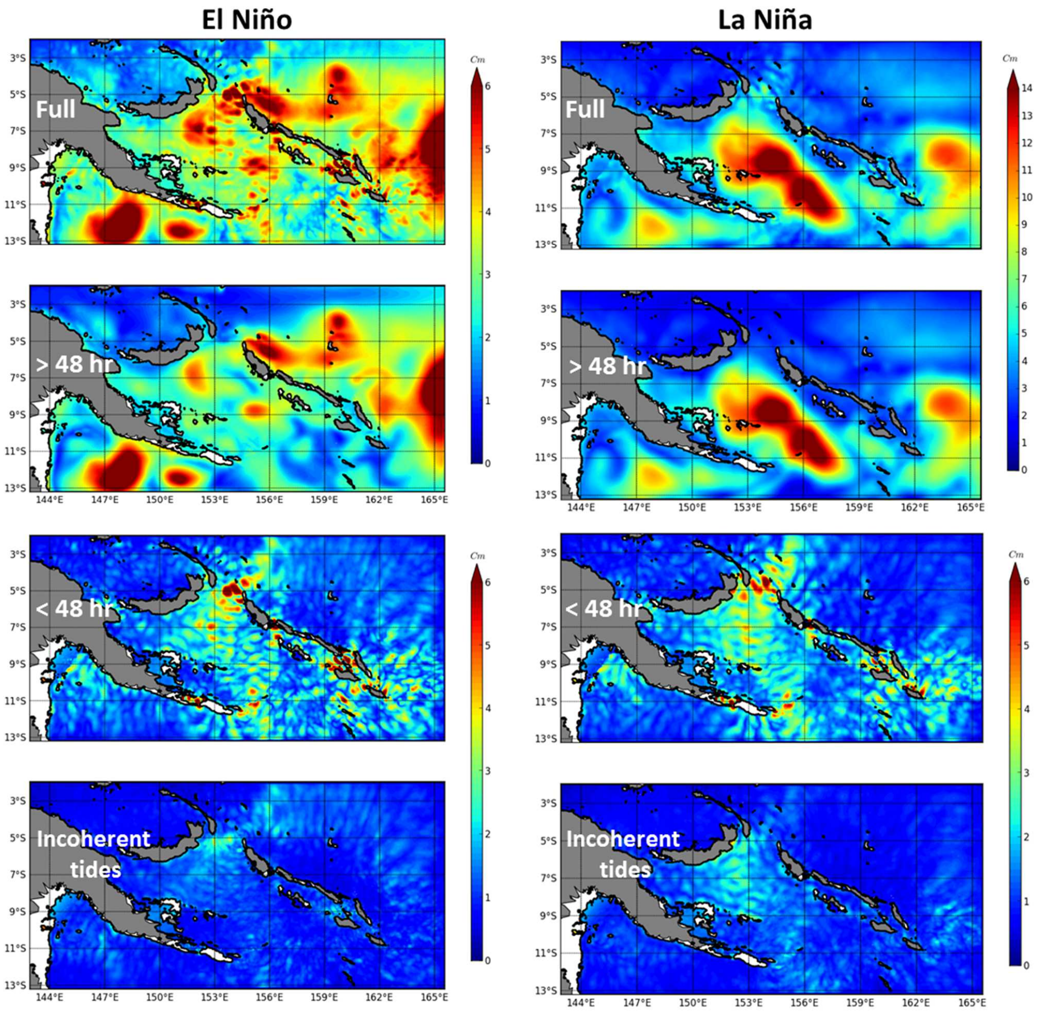

Figure 3: Root-mean-square of SSH variability for the 3-month periods of the El Niño state (left column) and of the La Niña state (right column). Unit is in cm. The top panel is the full SSH variance, the second panel is the mesoscale variability (periods > 48h), the third panel is the high frequency variability (periods < 48h), dominated by the internal tides (both coherent and incoherent components) and the bottom panel is the incoherent internal tide variability. Note the change of colorbar for the full and mesoscale variability of the La Niña period. Isobathymetric lines are from the NOAA/ETOPO2v2 bathymetric file from the Smith & Sandwell database (doi: 10.7289/V5J1012Q).

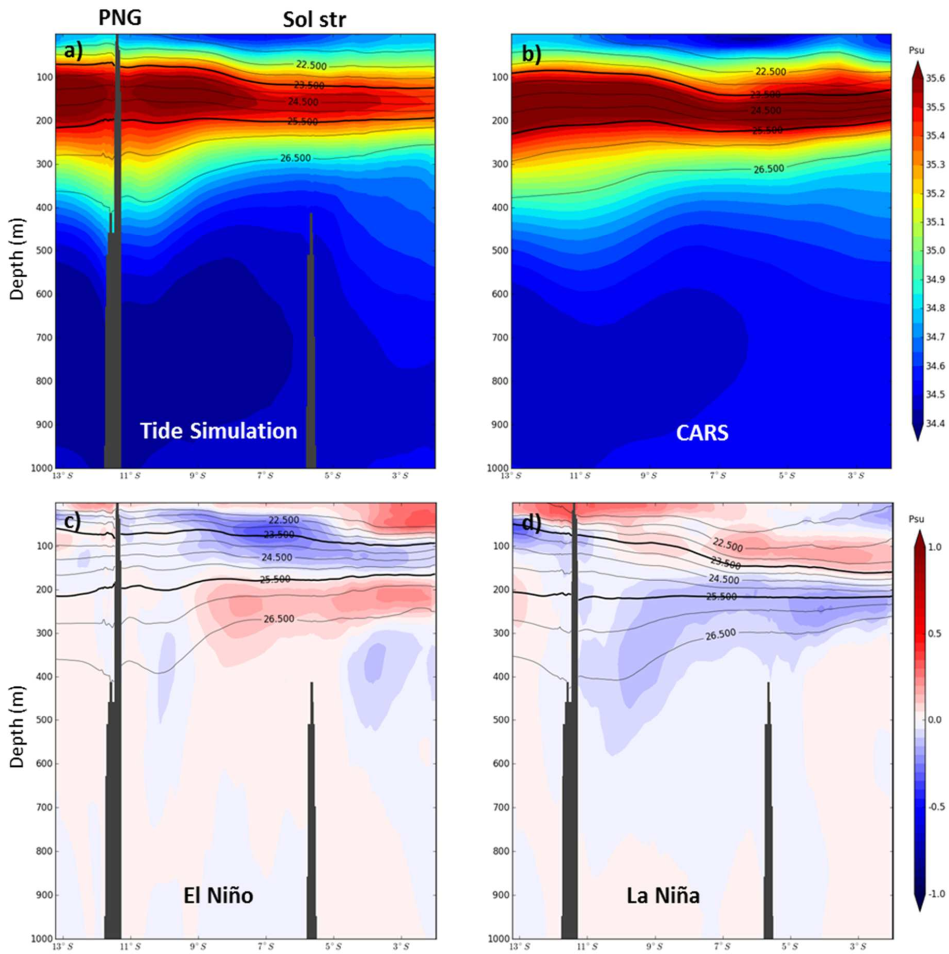

Figure 4: Latitude/depth section at 154°E of mean salinity from a) the R36Td simulation, b) CARS climatology, and of salinity anomalies for the 3 month c) El Niño period and d) La Niña period, relative to the full R36Td period. The Solomon Sea section is between the topographic features (vertical black lines) at 12°S and 6°S.

https://doi.org/10.5194/os-2019-94
Preprint. Discussion started: 26 September 2019

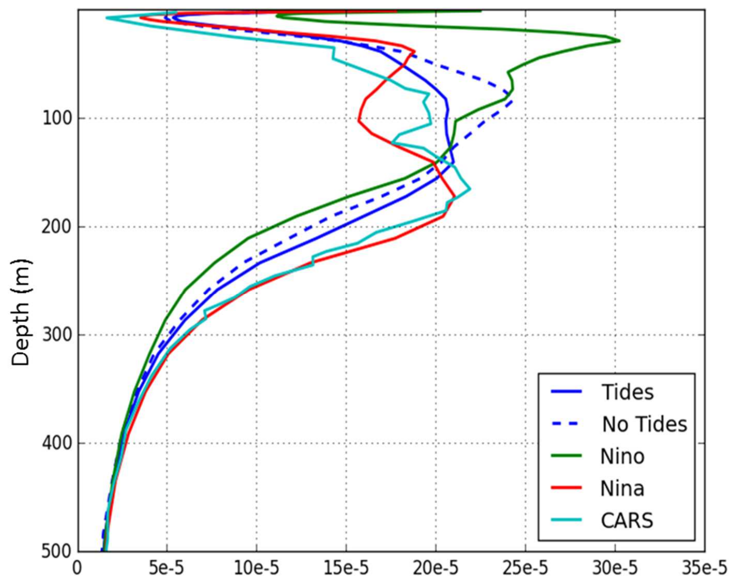

Figure 5: Mean N^2 profile averaged for the Solomon Sea section at 154°E from CARS climatology (Cyan), and from the R36Td TIDES simulation averaged over the entire 3-year period (blue), the 3-month El Niño period (green) and the 3-month La Niña period (red). The dash blue line is for the R36d NOTIDES simulation averaged over the entire 3-year period. Unit is in s^{-1}.

https://doi.org/10.5194/os-2019-94
Preprint. Discussion started: 26 September 2019

Ocean Science
Discussions
Open Access
EGU

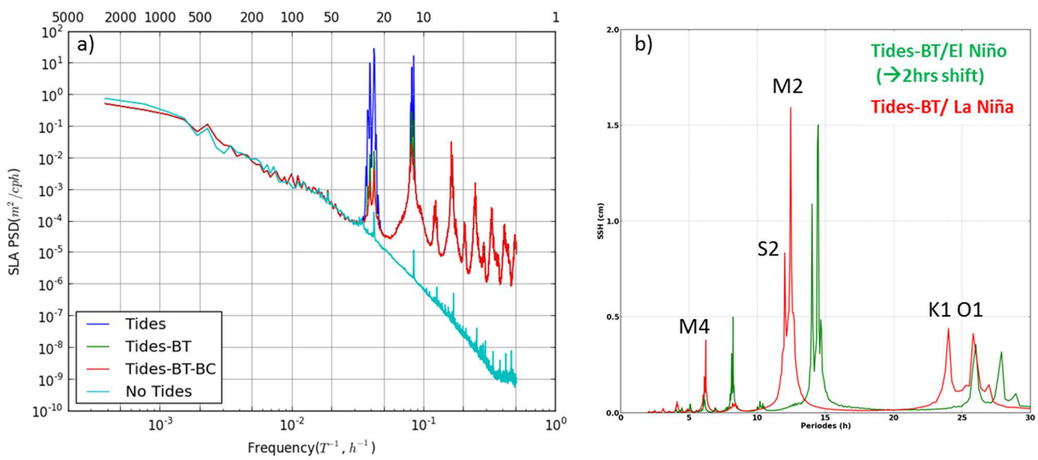

Figure 6: a) SSH frequency spectra averaged over the Solomon Sea area based on the 3 month hourly outputs of the El Niño period for the R36h simulation (No tides, in cyan), for the R36Th simulation including barotropic and baroclinic tides (Tides, in blue), baroclinic tides only (Tides-BT, in green), incoherent baroclinic tides only (Tides-BT-BC, in red). b) Zoom on SSH frequency spectra showing the diurnal, semidiurnal, and quart diurnal signature of baroclinic tides calculated during the El Niño period (in red) and the La Niña period (in green). For clarity the green spectrum is shifted by 2 hours.

https://doi.org/10.5194/os-2019-94
Preprint. Discussion started: 26 September 2019

Ocean Science
Discussions
Open Access
EGU

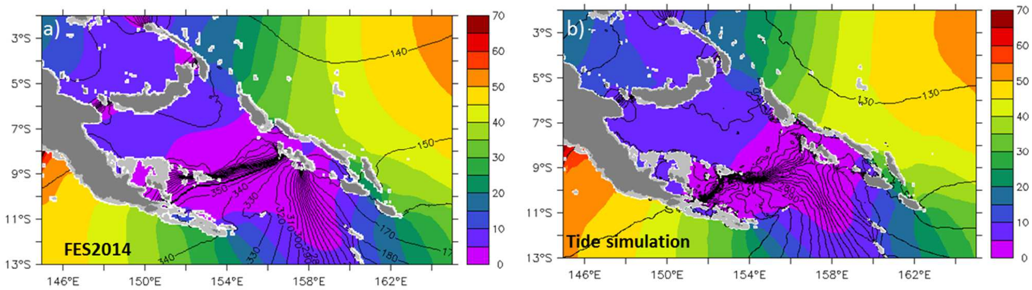

Figure 7: SSH M2 barotropic tide from a) FES2014, and b) the R36Th simulation. Amplitude is in color (unit in cm) and the contours are phase lines. Isobathymetric lines are from the NOAA/ETOPO2v2 bathymetric file from the Smith & Sandwell database (doi: 10.7289/V5J1012Q).

https://doi.org/10.5194/os-2019-94
Preprint. Discussion started: 26 September 2019

Ocean Science
Discussions

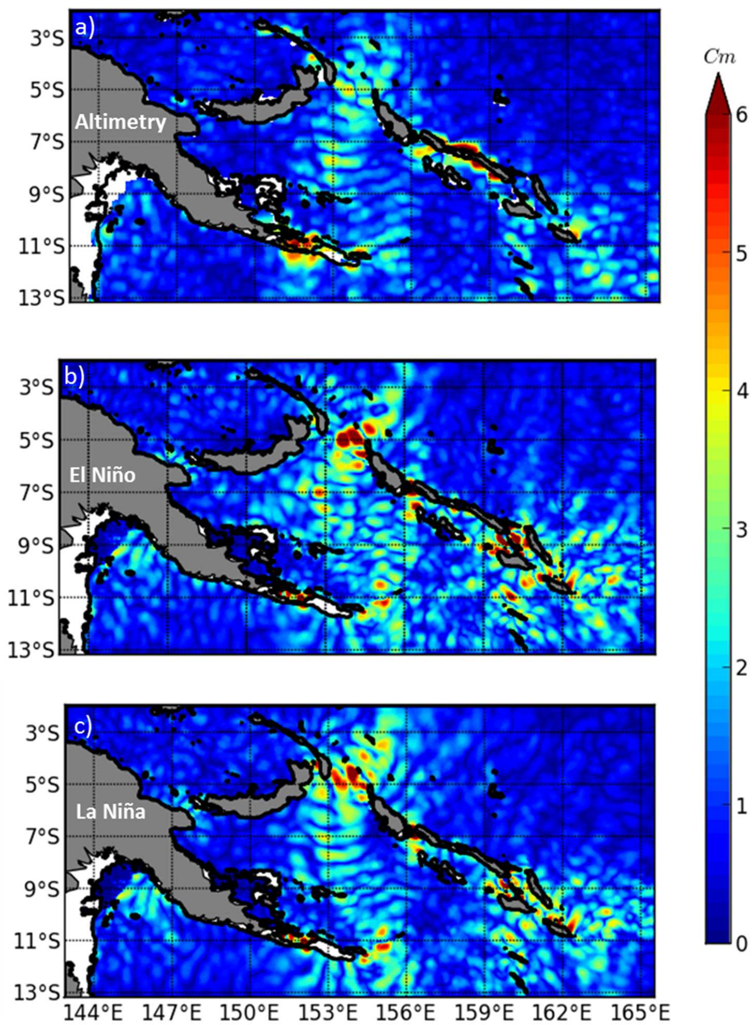

1093

1094 Figure 8: SSH amplitude of the stationary M2 baroclinic tide as estimated from a) altimetry by Ray and
1095 Zaron (2016), the R36Th simulations during the 3-months of b) the El Niño period, and c) the La Niña
1096 period. Unit in cm. Isobathymetric lines are from the NOAA/ETOPO2v2 bathymetric file from the Smith
1097 & Sandwell database (doi: 10.7289/V5J1012Q).

1098

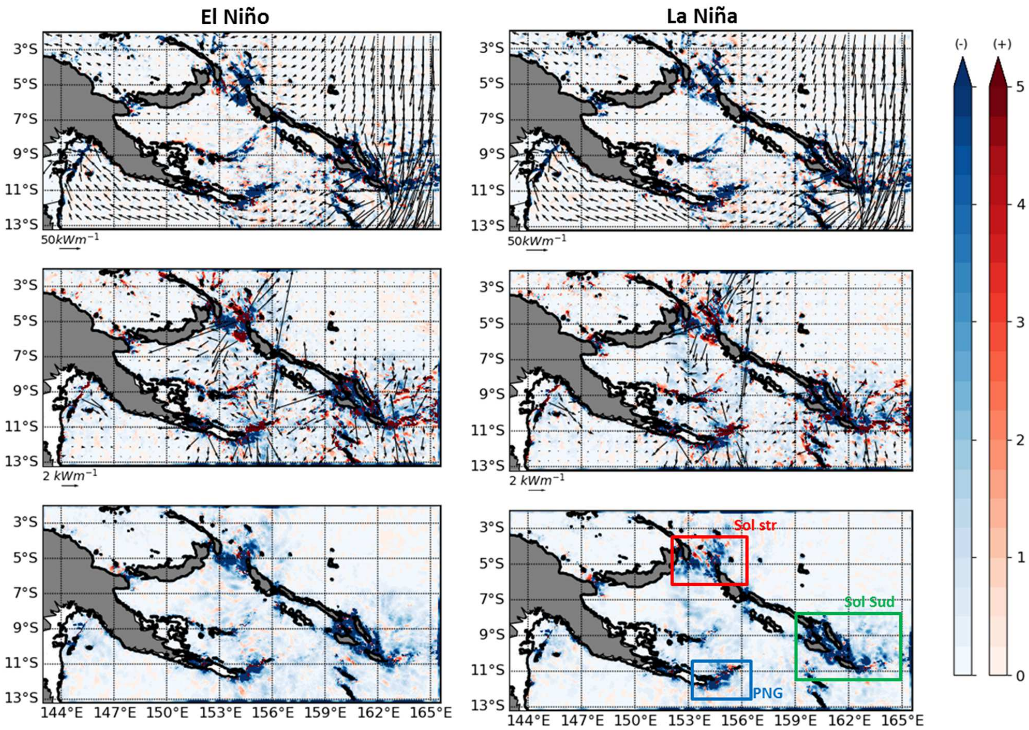

Figure 9: Conversion rate (top), the baroclinic flux divergence (middle), and the dissipation rate (bottom) for the M2 harmonic (negative values shaded in blue, positive values in red, unit: Wm^{-2}). The corresponding barotropic and baroclinic energy flux are superimposed with arrows in the top and middle panels, with a scaling of 50 kWm^{-1} and 2 kWm^{-1}, respectively. The left column corresponds to the El Niño period and the right column to the La Niña period. The boxes define the different generation areas where energetics are quantified in Table 1. Isobathymetric lines are from the NOAA/ETOPO2v2 bathymetric file from the Smith & Sandwell database (doi: 10.7289/V5J1012Q).

https://doi.org/10.5194/os-2019-94
Preprint. Discussion started: 26 September 2019

Ocean Science
Discussions
Open Access

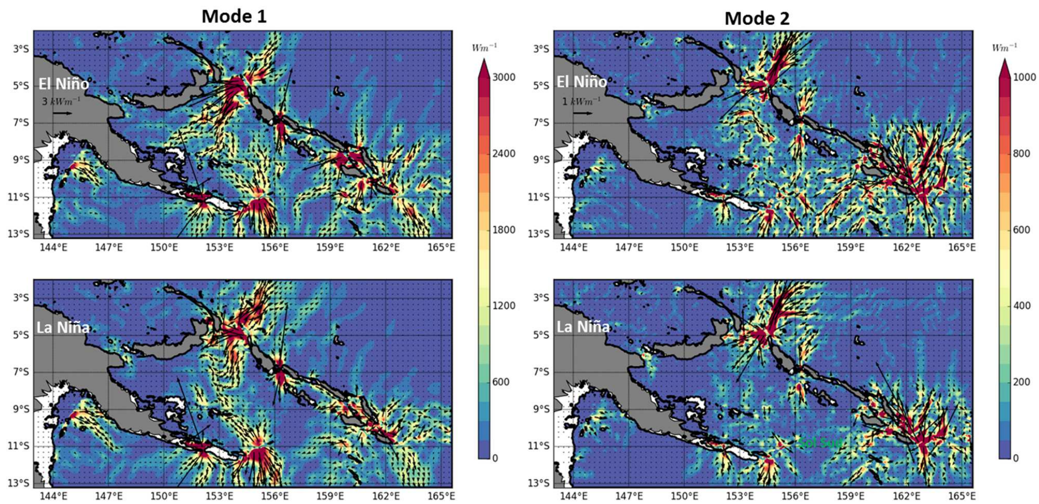

Figure 10: Modal decomposition of the M2 energy flux during the 3-month El Niño (top) and La Niña (bottom) periods, corresponding to mode 1 (left), and mode 2 (right). The shading is the amplitude (unit in Wm^{-1}). Isobathymetric lines are from the NOAA/ETOPO2v2 bathymetric file from the Smith & Sandwell database (doi: 10.7289/V5J1012Q).

https://doi.org/10.5194/os-2019-94
Preprint. Discussion started: 26 September 2019

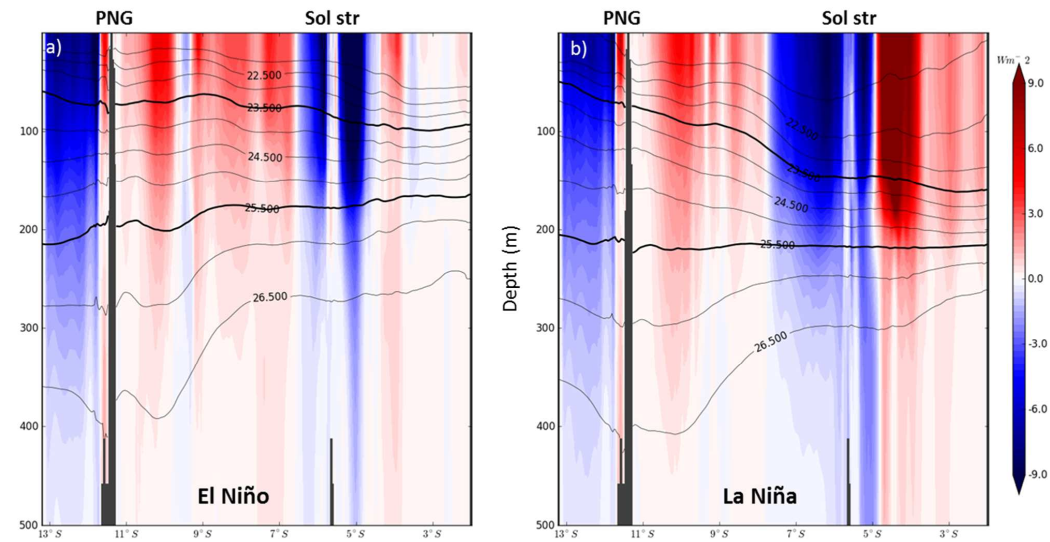

Figure 11: Vertical section at 154°E of the mean meridional energy flux estimated during a) El Niño state and b) La Niña state (unit in Wm^{-1}). The corresponding isopycnals are in contours; with σ = 23.5 and σ=24.5 in bold.

https://doi.org/10.5194/os-2019-94
Preprint. Discussion started: 26 September 2019

Ocean Science
Discussions

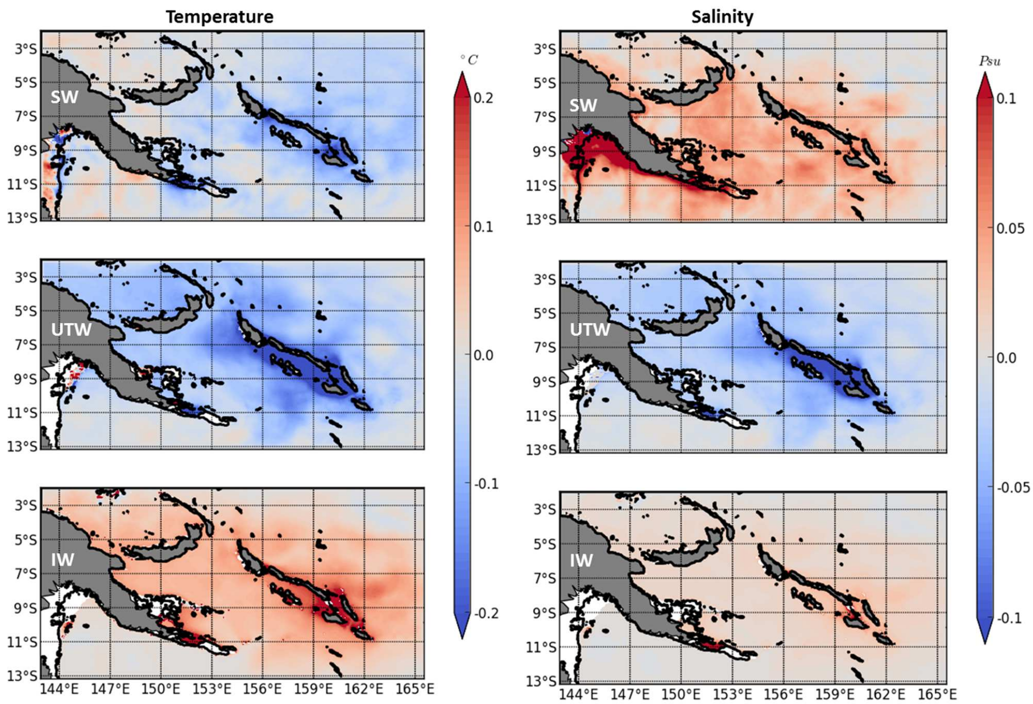

1134

1135

1136 Figure 12: Mean difference in temperature (left, unit in °C) and salinity (right) between the simulation
1137 with tides and the simulation without tides (TIDES-NOTIDES) for the surface waters (SW, top), the
1138 upper thermocline waters (UTW, middle), and the intermediate waters (IW, bottom). The density
1139 range for these water masses are defined in the text. Isobathymetric lines are from the
1140 NOAA/ETOPO2v2 bathymetric file from the Smith & Sandwell database (doi: 10.7289/V5J1012Q).

1141

https://doi.org/10.5194/os-2019-94
Preprint. Discussion started: 26 September 2019

Ocean Science
Discussions
Open Access

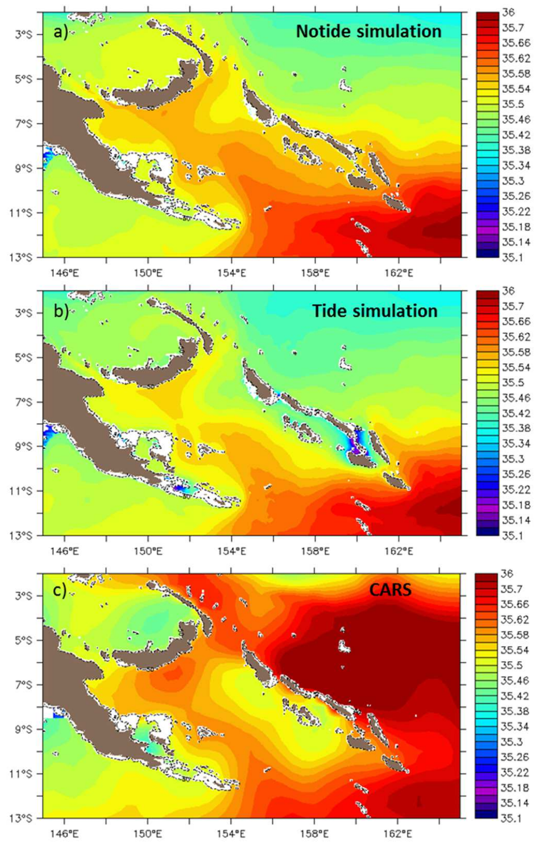

Figure 13: Mean salinity distribution in the UTW waters from the 3-year a) NOTIDE simulation, b) TIDE simulation, and c) the multi-decadal CARS climatology. Isobathymetric lines are from the NOAA/ETOPO2v2 bathymetric file from the Smith & Sandwell database (doi: 10.7289/V5J1012Q).

https://doi.org/10.5194/os-2019-94
Preprint. Discussion started: 26 September 2019

Ocean Science
Discussions
Open Access
EGU

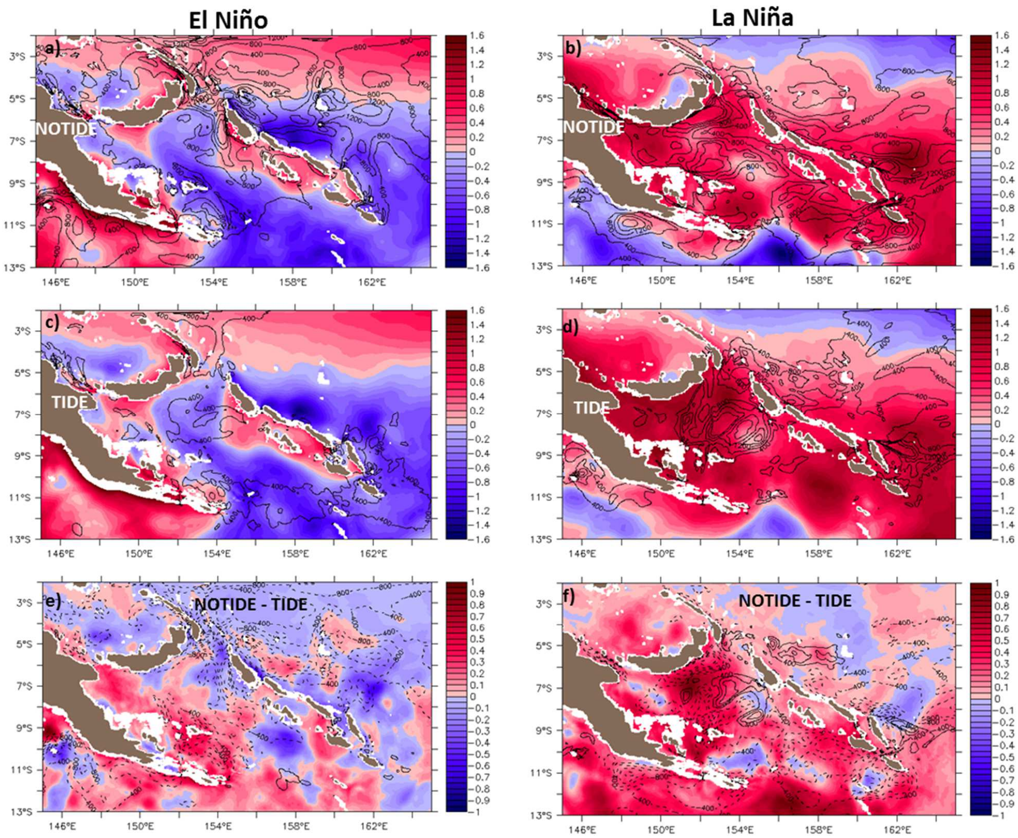

Figure 14: Temperature anomalies at 30 m depth relative to the 3 year mean average (shading, °C) over the El Niño period (left) and the La Niña period (right) for the NOTIDE simulation (a and b) and the TIDE simulation (c and d). Superimposed contours are the corresponding EKE field. EKE contours are plotted for values higher than 400 cm^2/s^2, every 400 cm^2/s^2. Bottom panels : difference in SST (shading, °C) and in EKE (contour, cm^2/s^2) between the TIDE and NOTIDE simulations averaged over e) the El Niño period, and f) the La Niña period. The black line and black dash contours are for positive and negative EKE differences, respectively; and contours are plotted every 400 cm^2/s^2. Isobathymetric lines are from the NOAA/ETOPO2v2 bathymetric file from the Smith & Sandwell database (doi: 10.7289/V5J1012Q).